

The cool core state of *Planck* SZ-selected clusters versus X-ray selected samples: evidence for cool core bias.

M. Rossetti^{1,2*}, F. Gastaldello¹, D. Eckert³, M. Della Torre², G. Pantiri²,
P. Cazzoletti^{2,4}, S. Molendi¹

¹*INAF, Istituto di Astrofisica Spaziale e Fisica Cosmica, via Bassini 15, 20133 Milano, Italy*

²*Dipartimento di Fisica, Università degli Studi di Milano, via Celoria 16, 20133, Milano, Italy*

³*University of Geneva, Department of Astronomy, 16, Ch. d'Ecogia, 1290, Versoix, Switzerland*

⁴*Max Planck Institute for Extraterrestrial Physics, Giessenbachstraße, 85748 Garching, Germany*

Accepted XXX. Received YYY; in original form ZZZ

ABSTRACT

We characterized the population of galaxy clusters detected with the Sunyaev-Zeldovich (SZ) effect with *Planck* by measuring the cool core state of the objects in a well-defined subsample of the *Planck* SZ catalogue. We used as indicator the concentration parameter (Santos et al. 2008). The fraction of cool core clusters is 29 ± 4 per cent and does not show significant indications of evolution in the redshift range covered by our sample. We compare the distribution of the concentration parameter in the *Planck* sample with the one of the X-ray selected sample MACS (Mann & Ebeling 2012): the distributions are significantly different and the cool core fraction in MACS is much higher (59 ± 5 per cent) than in *Planck*. Since X-ray selected samples are known to be biased towards cool cores due to the presence of their prominent surface brightness peak, we simulated the impact of the “cool core bias” following Eckert et al. (2011). We found that this bias plays a large role in the difference between the fractions of cool cores in the two samples. We examined other selection effects that could in principle affect SZ-surveys against cool cores but we found that their impact is not sufficient to explain the difference between *Planck* and MACS. The population of X-ray underluminous objects, which are found in SZ-surveys but missing in X-ray samples (Planck Collaboration XXVII 2016), could possibly contribute to the difference, as we found most of them to be non cool cores, but this hypothesis deserves further investigation.

Key words: galaxies: clusters: general, galaxies: clusters: intracluster medium

1 INTRODUCTION

It is often difficult to derive the statistical properties of a population of celestial sources from an observed sample which is a particular realization of the underlying population. Indeed, one has to be sure that the sample under analysis is representative and unbiased with respect to selection effects, i.e. that the method that was used to detect objects, and eventually to further select them, does not influence the properties that we want to analyze. Galaxy clusters are no exception to this rule.

Ever since the beginning of X-ray astronomy, X-ray observations have provided an efficient way to detect and characterize clusters. Many clusters catalogues (i.e. REFLEX, Böhringer et al. 2004, NORAS Böhringer et al.

2000, HIFLUGCS Reiprich & Böhringer 2002, REXCESS Böhringer et al. 2007, MACS Ebeling et al. 2001) have been built basing on the ROSAT All Sky Survey (RASS), which was excellent in terms of sky coverage but limited in depth. X-ray surveys aimed at detecting extended sources, such as galaxy clusters, may become “surface brightness limited” rather than “flux limited” at faint fluxes (Rosati et al. 2002; Pierre et al. 2016). Indeed, realistic X-ray surveys can detect extended objects up to a “detection radius” where they exceed the background level. It is thus easier to detect a cluster with a prominent surface brightness peak than an object with a shallower profile, even if they have the same flux when integrated to a physically relevant radius (i.e. R_{500}), typically larger than the detection radius. This selection bias which affects X-ray surveys of galaxy clusters is also known as “cool core bias” (Eckert et al. 2011) and it was early recognized in the first *Einstein* surveys of

* E-mail: rossetti@iasf-milano.inaf.it

galaxy clusters (Pesce et al. 1990 and references therein). “Cool core” (CC hereafter) clusters are observationally characterized by a prominent central surface brightness peak associated to a temperature decrease in the inner regions and are usually considered as relaxed objects. Eckert et al. (2011) have shown that their number is overestimated in X-ray selected clusters samples (HIFLUGCS) because of their prominent surface brightness peak. A further bias is due to the higher luminosity of CC clusters with respect to NCC at a given mass, which makes the detection rate of CC higher than fainter NCC objects, in a flux limited sample suffering from the Malmquist bias (Hudson et al. 2010). Thus the ratio between CC and NCC objects, which depends strongly on CC formation scenarios and on the models of cluster evolution, is likely over-estimated in X-ray selected samples.

Over the last decade, an alternative method to search for galaxy clusters has received growing attention: the Sunyaev-Zeldovich effect (SZ hereafter Sunyaev & Zeldovich 1970; Sunyaev & Zeldovich 1972), with the publications of the first large catalogues of galaxy clusters from different experiments, containing from one hundred to more than one thousand objects (Hasselfield et al. 2013; Bleem et al. 2015; Planck Collaboration XXIX 2014; Planck Collaboration XXVII 2016). The SZ surface brightness does not depend on the redshift of the source, allowing us in principle to detect all the clusters in the universe above a given signal, regardless of their distance, and to build virtually mass limited samples of galaxy clusters. Actually the finite spatial resolution of real instruments limits the detection of the most distant objects (especially for *Planck* whose lowest energy channel used for SZ measurement has a beam size of 10 arcmin) but the distribution of clusters in the mass-redshift plane is definitely flatter for SZ-selected samples than for X-ray samples. **Indeed, SZ surveys have detected more than 450 clusters at $z > 0.5$, significantly increasing the number of known objects in this redshift range, which was limited to a few tens of clusters in X-ray catalogues before them (75 in MCXC, Piffaretti et al. 2011).**

Simulations have shown that SZ quantities do not strongly depend on the dynamical state of the clusters (Motl et al. 2005), showing only a modest effect of less than 10% due to mergers (Krause et al. 2012; Battaglia et al. 2012). This is supported observationally by the small scatter in the scaling relation between the SZ total signal Y and the mass (e.g. Planck Collaboration XX 2014 and references therein). Moreover, Planck Collaboration XXVII (2016) showed with MonteCarlo simulations that the morphology of the source, which is in general more irregular and disturbed for interacting systems, has negligible impact in the detection procedure in the *Planck* survey. In principle, CC bias may play a role also in SZ surveys: CC clusters feature a prominent peak in the pressure profiles (Planck Collaboration. V, 2013), which results in an increase in the central value of the Comptonization parameter $y \propto \int Pd\ell$ (Pipino & Pierpaoli 2010). However, simulations have shown this effect to be small, especially for *Planck* whose beam size is larger than the typical cluster size and is more sensitive to the total SZ signal rather than to its central value (Pipino & Pierpaoli 2010; Lin et al. 2015).

In a recent paper (Rossetti et al. 2016, Paper I hereafter),

we showed that the dynamical state of *Planck* SZ-selected clusters is significantly different than in X-ray surveys. We measured an indicator of dynamical activity ($D_{X,BCG}$, the projected offset between the position of the X-ray peak and the one of the brightest cluster galaxy) for a representative subsample of *Planck* clusters (Planck Collaboration XX 2014) and we compared its distribution to the one of the same indicator in several X-ray selected samples available in the literature. The distributions are significantly different and the fraction of dynamically relaxed objects is smaller in the *Planck* sample than in X-ray selected samples, confirming the early impression that many *Planck*-selected objects are dynamically disturbed systems (Planck Collaboration, IX, 2011). In Paper I, we suggested that the origin of this discrepancy may be due to the CC-bias affecting X-ray surveys, since dynamically relaxed objects usually host cool cores. However, we could not verify this hypothesis as $D_{X,BCG}$ is not a direct indicator of the presence of a peaked surface brightness profile, although it shows correlations with several cool core indicators (Sanderson et al. 2009). To test this hypothesis one would need to measure the presence and strength of the surface brightness peak in large SZ and X-ray samples and compare them. A first result in this direction has been presented by Semler et al. (2012), who measured the concentration parameter (Santos et al. 2008), a CC indicator directly related to the strength of the surface brightness peak, for a small sample of clusters detected by SPT (13 objects). They compare the distribution of this indicator in their sample with the one in the X-ray selected 400d sample (Burenin et al. 2007) and found them to be consistent, but given **their small number of objects** they could constrain only the fraction of CCs between 7 and 59 %. More recently, McDonald et al. (2013) measured the concentration parameter, as well as other CC indicators, for a larger SPT sample but do not directly make a comparison with X-ray samples. Although it was not the main objective of their paper, Mantz et al. (2015) provided a first significant result, finding that the fraction of objects with a peaked surface brightness profile is significantly higher in X-ray selected samples than in SZ samples, using SPT and a small (30 objects) subset of the early *Planck* catalogue (Planck Collaboration, VIII. 2011). Conversely, the recent comparison by Nurgaliev et al. (2016) between the SPT SZ sample and the X-ray selected 400d catalogue (Burenin et al. 2007) does not address directly the role of CC-bias as it is based on morphological indicators which measure the deviation from symmetry of the cluster images and thus compare the dynamical state, as we have also done in Paper I.

The aim of the present paper is to directly address the origin of the discrepancy in the dynamical state that we found in Paper I and to test the hypothesis that it is due to the CC-bias. We use as CC indicator the concentration parameter (Santos et al. 2008), since it directly measures the strength of the SB peak. We measure it for a large sample of SZ-selected clusters drawn from the *Planck* catalogue and consistently for the X-ray selected MACS sample (Mann & Ebeling 2012). The outline of the paper is as follows. In Sec. 2 we present our samples while in Sec. 3 we describe the reduction and analysis of *Chandra* and *XMM-Newton* data, that we applied to both samples. We present our results and compare the

distributions in Sec. 4, comparing it also with previous results and other samples available in the literature. In Sec. 5 we discuss the role of CC-bias, trying to reproduce our results with simulations. Finally, we discuss other possibilities in Sec. 6. In this paper, we assume a Λ -CDM cosmology with $H_0 = 70 \text{ km s}^{-1} \text{ Mpc}^{-1}$, $\Omega_m = 0.3$ and $\Omega_\Lambda = 0.7$.

2 THE SAMPLES

2.1 *Planck* cluster sample

The starting point of our SZ-selected sample is the *Planck* cosmology sample (PSZ1-cosmo), which has been used for the cosmological analysis with cluster number counts described in [Planck Collaboration XX \(2014\)](#). It is a high-purity subsample built from the first release of the *Planck* catalogue of SZ sources ([Planck Collaboration XXIX 2014](#)), containing all the detection with highest signal-to-noise ratio ($S/N > 7$) after the application of a mask, that excludes the galactic plane and point sources and leaves 65% of the sky for the survey. It contains 189 clusters: all of them have been confirmed at other wavelengths and redshifts have been associated to each cluster. The properties of the sample and its completeness are described in detail in [Planck Collaboration XX \(2014\)](#). The PSZ1-cosmo sample has been almost completely followed-up in X-rays with either *Chandra* or *XMM-Newton* and is thus the ideal starting point to measure the concentration parameter (Sec. 3.3) of *Planck*-selected objects. The larger and more recent second release of the *Planck* SZ catalogue (PSZ2, [Planck Collaboration XXVII 2016](#)) has not benefited yet of a similar follow-up campaign and the analysis of this sample would thus be strongly incomplete.

We used *Chandra* data as a reference because better suited for the measurement of concentration parameters given the excellent spatial resolution. We measured concentration parameters for 154 objects with *Chandra* at $z > 0.07$, using this redshift as a lower limit to accommodate 400 kpc within the *Chandra* ACIS-I field of view. For 10 objects at $z > 0.07$ we measured concentration parameters with the *XMM-Newton* data, as *Chandra* data were not available in the archive. For 5 objects in the redshift range 0.03 – 0.07 we used *XMM-Newton* data, exploiting its larger field of view to cover the cluster region used in the definition of the concentration parameter (Sec. 3.3). The remaining objects for which observations are potentially available but not used here are: 8 clusters with *Chandra* data planned or still proprietary as of July 2016, 4 clusters with *XMM-Newton* data at $z < 0.03$ (not completely covered even with *XMM-Newton*) and 4 clusters at $z > 0.35$, for which the core region used in our indicator is not resolved with *XMM-Newton* (Sec. 3.3). Our final sample is thus composed of 169 clusters in the redshift range 0.04–0.87 with a median $z = 0.18$ and in the mass range $(2 - 12) \times 10^{14} M_\odot$ (median $M_{500} = 6.2 \times 10^{14} M_\odot$).

2.2 MACS sample

In Paper I, we compared the distribution of our dynamical indicator in the *Planck* sample with the one of three X-ray selected samples (HIFLUGCS, REXCESS and MACS). We

showed that MACS is the most suited for the comparison with *Planck* among those samples, since its redshift and mass distributions are more similar to the ones of the PSZ1-cosmo sample. Actually, the sample that we used in Paper I is not the original MACS sample (whose selection criteria are described in [Ebeling et al. 2001](#)) but its extended version described in [Mann & Ebeling 2012](#) (ME-MACS hereafter). Both MACS and ME-MACS are drawn from the RASS Bright Source Catalogue ([Voges et al. 1999](#)), with a flux limit $f_{\text{RASS}}[0.1 - 2.4 \text{ keV}] > 1 \times 10^{-12} \text{ erg cm}^{-2} \text{ s}^{-1}$. The main difference is that MACS is limited by definition to the most distant systems ($z > 0.3$), while ME-MACS extends to lower redshifts ($z > 0.15$) and has an additional luminosity cut $L_{\text{RASS}}[0.1 - 2.4 \text{ keV}] > 5 \times 10^{44} \text{ erg s}^{-1}$. The ME-MACS sample is a well-defined purely X-ray selected sample, based on a flux limited survey, and it is thus well suited for a comparison between the X-ray and SZ selection. Moreover, its redshift distribution is more similar to the redshift distribution of the *Planck* sample with respect to the original MACS and we thus decided to use it in our analysis. Finally, 104 out of the 129 clusters meeting the ME-MACS selection (listed in [Mann & Ebeling 2012](#)) have public *Chandra* observations that we used to measure the concentration parameter (Sec. 3.3).

2.3 Mass and redshift distributions

In Fig. 1, we show the redshift and mass distribution of the *Planck* and ME-MACS samples. As in Paper I, we estimate the masses of the ME-MACS clusters using the $L-M$ scaling relation in [Pratt et al. \(2009\)](#). By construction, the minimum redshift of the ME-MACS sample is 0.15, thus the median value of the ME-MACS sample ($z = 0.35$) is larger than in the PSZ1 sample and the two distributions are significantly different. Also the mass distributions appear different: objects with $M < 5 \times 10^{14} M_\odot$ are found only in the *Planck* sample and correspond to the low-redshift objects which are missing by construction in ME-MACS. To minimize the difference in the two samples we define a subsample of the *Planck* catalogue by imposing $z > 0.15$: with this choice we have a subsample of 103 objects, with median redshift 0.25 and median mass $7.1 \times 10^{14} M_\odot$.

3 DATA ANALYSIS

3.1 *Chandra* data reduction

We analyzed *Chandra* data with the CIAO software 4.6 using CALDB version 4.6.1, reprocessing data from the level 1 event files and following the standard data reduction threads¹. We reprocessed event files using the `chandra_repro` tool with standard corrections. We used as background files the blank-sky fields provided in the CALDB database, that we reprocessed, reprojected and renormalized² to match observations. We detected point sources using the `wavdetect` tool and we extracted a light

¹ <http://cxc.harvard.edu/ciao/threads/index.html>

² We compute the renormalization factor as the ratio between the source and background count rate in the 9 – 12 keV band.

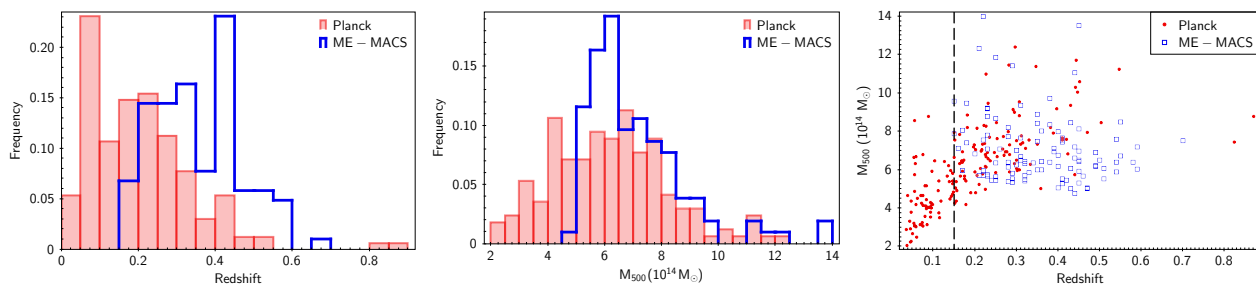


Figure 1. Distribution of redshift (left), mass (middle) and $M - z$ plane (right) in the *Planck* and ME-MACS samples.

curve excluding them to identify and remove periods of enhanced background. We used the `fluximage` tool to produce images in the 0.7 – 2 keV bands and the appropriate exposure maps. We cleaned the images from point sources using `dmfilth` by replacing the count rates in the point source region with the mean value in a surrounding annulus. From the rescaled background files we extract images in the same energy band and with the same size of the cluster images that we use for background subtraction. As our analysis is based on flux measurements in the soft band and in the central regions of the clusters (Sec. 3.3), where the source outshines the background, possible systematics in the background renormalization and subtraction do not affect significantly our results.

3.2 *XMM-Newton* data reduction

We reduced *XMM-Newton* observations with the SAS software 14.0 starting from the raw files in the archive, which we reprocessed to produce calibrated event files. We used the Extended Source Analysis Software (ESAS, Snowden et al. 2008) to filter periods affected by soft proton flares and to produce images in the 0.5 – 2.5 keV band for each EPIC detector. We also computed the appropriated exposure maps and a model image of the instrumental background for each detector. We then combined the images with the `comb` ESAS tool to produce EPIC images.

3.3 Measuring the concentration parameter

For each cluster in the PSZ1 and ME-MACS sample with available X-ray images, we computed the concentration parameter introduced by Santos et al. (2008):

$$c = \frac{F(r < 40\text{kpc})}{F(r < 400\text{kpc})}, \quad (1)$$

where $F(r < 40 \text{ kpc})$ is the flux within 40 kpc from the centre (representing the core region) and $F(r < 400 \text{ kpc})$ is the flux within 400 kpc, representing the cluster emission. Santos et al. (2008) introduced this parameter to discriminate CC and NCC objects also at high redshift and using observations with poor statistics. They tuned the choice of the radii of the two regions (40 and 400 kpc) to separate more efficiently CC from NCC and to be able to compute c with *Chandra* data both for their high-redshift sample ($z > 0.7$) and for intermediate redshift clusters ($0.1 < z < 0.3$). Since the clusters in our samples span a similar redshift range, we decided to use the original definition of the parameter which is furthermore the most used in the literature.

To compute the concentration parameter as in Eq. 1, we calculate the intensity of the cluster emission using the background-subtracted and exposure corrected *Chandra* or *XMM-Newton* images (Sec. 3.1 and 3.2). We take into account the poissonian noise in both source and background images and compute the error on the concentration parameter, which is typically of the order of 5%. To define the two regions of interest, we need to fix a centre for the two circles and we decided to use the peak of the X-ray images, selected as the brightest pixels in the clean image after masking the point sources and smoothing it with a Gaussian with a FWHM of 7 arcseconds to reduce statistical fluctuations. When multiple observations are available for the same object, we estimated the peak from the mosaic image **to minimize the impact of statistical fluctuations especially for disturbed objects that do not feature a clear peak**. We measured the total number of net counts and its error within 40 kpc and 400 kpc, correcting for background, vignetting (through the exposure map) and CCD gaps when they intersect the regions of interest, and compute their ratio. When multiple observations are available for the same object, we measured the concentration parameter on each observation and compute their weighted mean. We tested that this procedure provides consistent results than measuring the concentration parameter directly on the mosaic image. We applied the same procedure for the clusters in our PSZ1 sample and on the ME-MACS: we provide the estimated values in Table 1 and 2.

Santos et al. (2010) show that for CC clusters the amount of K-correction is different for the inner 40 kpc, where the temperature is lower, than in the larger 400 kpc region and that this effect reduces the concentration parameter at high redshifts. They estimate this effect to reach 15% for strong CCs at $z = 1$, depending on the temperature in the inner region. As we do not have temperature profiles for all the clusters in our samples, we could not compute the correction factors directly for all objects. Nonetheless, we could estimate an upper limit to the intensity of this effect, by assuming for all CC clusters in our sample a minimum temperature of one third of the virial temperature, which we estimated with the M-T scaling relation by Arnaud et al. (2005). We calculate the correction factor as described in Santos et al. (2010) and we find that the concentration parameters of CC clusters at a median $z = 0.25$ should be lower by $\approx 5\%$ with respect to their values at $z = 0$. Given the limited redshift range of our samples and the high temperature of the ICM for massive clusters, this correction is thus comparable or smaller than the statistical errors on the parameters. Nonetheless,

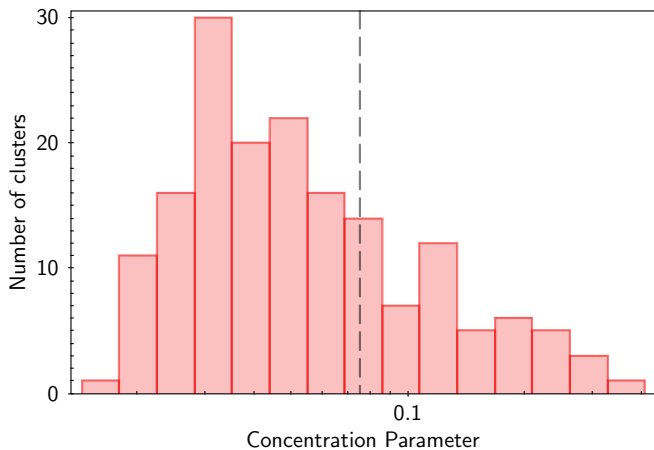


Figure 2. Distribution of the concentration parameter in the *Planck* sample. The vertical dashed line marks the threshold to separate CC ($c > 0.075$) from NCC ($c < 0.075$).

comparison with samples or subsamples in different redshift ranges should be taken with caution.

4 RESULTS

4.1 The distribution in the *Planck* sample

In Fig. 2, we show the histogram of the concentration parameter distribution in the *Planck* sample with logarithmic bins. The distribution features a single peak at low values of the concentration parameters with a tail extending to higher values. The median concentration parameter is $c = 0.0475$.

We classified objects into two classes, CC and NCC, using a threshold value $c = 0.075$. This value is based on Santos et al. (2008), who calibrated it with the cooling time, to separate NCC and “moderate CC”. We merged into a single CC class the “moderate CC” and “pronounced CC” classes of Santos et al. (2008). With this classification we find 49/169 CC in our sample, corresponding to a CC fraction of $(29 \pm 3)\%$, where we estimated the error with bootstrap resampling. If we consider only the subsample with $z > 0.15$, we find a consistent value $(29 \pm 4)\%$.

As discussed in Sec. 2.1, our *Planck* sample is not fully complete and we are missing 20 objects from the original *Planck* cosmology sample. Even in the unlikely case that all missing clusters are classified as CC, the CC fraction of the *Planck* sample would rise only up to 36%.

We divided the sample in redshift and mass subsamples to test for a possible evolution or mass dependence of the CC fraction, as measured by our indicator. The CC fractions for each subsample are shown in table 3. We do not find a significant variation of the CC fraction with redshift in the PSZ1 sample. However, this is not in contrast with the results found by McDonald et al. (2013), who showed a significant evolution of the CC fraction, as measured by the concentration parameter, in their sample drawn from the SPT SZ catalogue. In fact, the evolution in the SPT sample becomes evident only in redshift bins at $z > 0.3$, a redshift range where we have only 24 objects in our *Planck* sample. Indeed, at $z > 0.3$, we could measure a CC fraction of 29%

Subsample	CC fraction %
$z < 0.18$ (median)	27 ± 5
$z > 0.18$ (median)	30 ± 5
$z > 0.15$ (ME-MACS)	29 ± 4
$M < 6.5 \times 10^{14} M_{\odot}$	24 ± 4
$M > 6.5 \times 10^{14} M_{\odot}$	34 ± 5

Table 3. CC-fraction in redshift and mass subsamples of the *Planck* sample.

with an error of 9%, which does not allow us to draw any conclusion. Moreover, as discussed in Sec. 3.3 we could not apply the K-correction to our dataset and this prevents us from deriving strong constraints on the evolution of the CC fraction.

Concerning the mass dependence, we see a small difference in the CC fraction, with the low mass subsample featuring a lower CC fraction than the high mass subsample. Although this result is likely a statistical fluctuation (1.5σ), it is interesting to note that a similar behaviour has been found also by Mantz et al. (2015): using their SPT sample they find a higher fraction of “peaky” objects among hotter clusters, while they do not find a similar trend for X-ray selected samples. The opposite trend has in fact been noted in X-ray surveys, where low-mass objects are predominantly CC (e.g. Chen et al. 2007), possibly as a consequence of the CC bias (see discussion in Eckert et al. 2011). Nonetheless, an increasing CC-fraction with mass is not expected and, **under the hypothesis that CCs are relaxed systems**, seems to contradict the prediction of hydrodynamical simulations that find an increasing fraction of merging clusters as a function of mass (Fakhouri et al. 2010). We underline that this trend is poorly significant both in the *Planck* and SPT sample and needs to be verified with a larger number of objects, possibly SZ selected.

4.2 Comparison with ME-MACS

In Fig. 3 we compare the distribution of the concentration parameter of the *Planck* sample (described in Sec. 4.1) with the one in the ME-MACS sample. The distribution of the X-ray selected ME-MACS is qualitatively different from the one of the *Planck* sample: it shows two peaks, one for the NCC objects and one corresponding to CCs.

Most objects in ME-MACS are classified as CC and the CC fraction is $59 \pm 5\%$. We can compare it directly with the CC fraction in the *Planck* sample estimated with the same indicator and the same threshold (Sec. 4.1): the difference is significant at more than 5σ . The difference is still significant even when compared to the CC fraction in the *Planck* subsample with $z > 0.15$ ($29 \pm 4\%$). Even assuming that all the clusters which meet the ME-MACS criteria but do not have *Chandra* observations (Sec. 2.2) are NCC, the CC fraction would decrease only to 47%, larger at 3σ than the fraction in the *Planck* sample.

We can further apply statistical tests to compare the two distributions shown in Fig. 3 to assess that they are different independently of the choice of the threshold separating CC from NCC. We use the Kolmogorov-Smirnov test, which

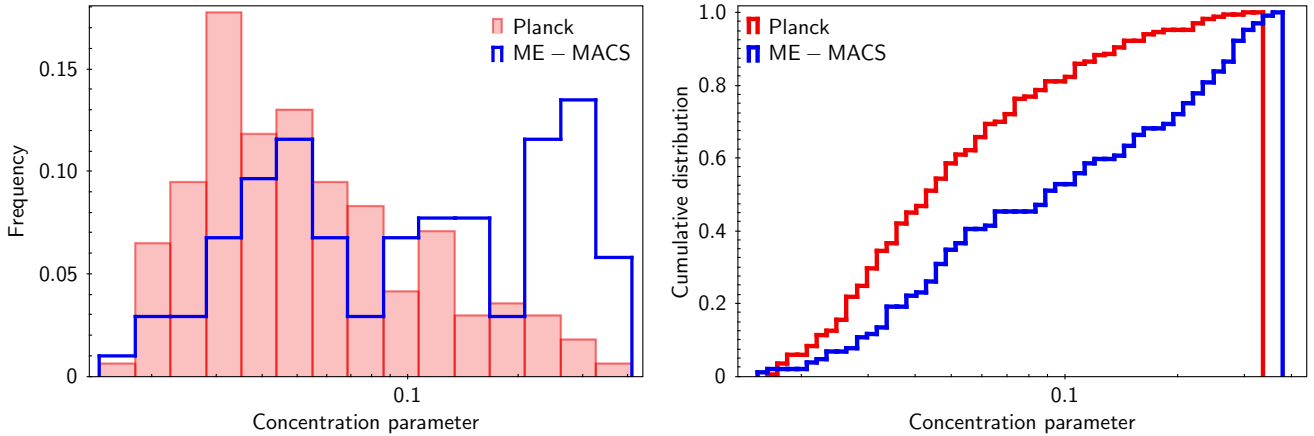


Figure 3. Histogram (left) and cumulative (right) distribution of the *Planck* (red) and ME-MACS (blue) samples.

measures the probability that the two samples are drawn from the same parent distribution. The KS statistic D , i.e. the supremum distance from the two cumulative distributions (Fig. 3), is 0.349, with a null-hypothesis-probability $p_0 = 1.68 \times 10^{-7}$, showing that the *Planck* and ME-MACS distributions are significantly different. If we consider only the *Planck* subsample with $z > 0.15$ (Sec. 2.3), the KS still returns a significant difference between the *Planck* and ME-MACS sample ($D = 0.334$ and $p_0 = 1.24 \times 10^{-5}$).

The result of the KS test is supported by the qualitative difference between the two distributions: two peaks seem present in the ME-MACS sample, whereas the distribution of *Planck* values looks more consistent with a peaked distribution with a tail at high concentration values, i.e. a positively skewed function. We tested these differences quantitatively performing a maximum likelihood fit for each of the two distributions on the unbinned data using the MCLUST package (Fraley & Raftery 2002; Fraley et al. 2012) and the FITDISTR function of the package MASS (Venables & Ripley 2002) in the software environment R version 3.2.2 (R Core Team 2015). The model-based clustering implemented in MCLUST is an algorithm for fitting normal mixture models, i.e. maximum likelihood fits are performed assuming a number from 1 to 9 normal components are present in the data. The function FITDISTR performs a maximum likelihood fit of the data to some probability distribution functions, either calculated using analytic formulae (as for example in the log-normal case) or computed by optimization of the likelihood. We chose for fitting two commonly used positively skewed functions: the Weibull and log-normal distributions. We performed model selection comparing the Bayesian Information Criterion (BIC, Schwarz 1978) defined as $\text{BIC} = 2\ln L - k\log(n)$ where L is the likelihood, k is the number of parameters of the model and n is the number of data points; $k\log(n)$ is the penalty term which compensates the difference in likelihood due to an increase in the number of fitting parameters. The best model is the one that maximizes the BIC. Commonly adopted thresholds for the difference in BIC values of two models are: a BIC difference of 0-2 is considered as weak evidence, 2-6 positive evidence, 6-10 strong evidence and > 10 as very strong evidence in favor of the model with the greater BIC value (Kass & Raftery 1995; Raftery 1995). We did not work on log space because the positively skewed

functions are not defined for negative values. For ME-MACS the result of the normal mixture model strongly disfavors a single Gaussian component, with a BIC value of 159.88 with respect to two Gaussian components with a BIC of 217.99. A three components Gaussian model has a BIC value of 219.88 so the improvement is not significant. The two components consist of 41 and 62 members with the separation at a value of 0.07 (see Fig. 4, left panel), which is similar to the threshold to separate CC and NCC that we adopted in our analysis. The fit with positively skewed functions returns BIC values of 203.70 and 202.23 for the log-normal and Weibull distributions respectively. Those models are therefore clearly disfavored with respect to a two components normal mixture model. For the *Planck* sample the model with the highest BIC value is the one with 3 Gaussian components, with a BIC of 610.20 which is significant with respect to a 2 components model which has a BIC of 597.63. The optimal partition returns three groups with 71, 59, and 39 members respectively with separations at values of the concentration parameters of 0.04 and 0.09 (see Fig. 5, left panel). The fit with a log-normal function returns a BIC value of 622.60 so this model is favored with strong evidence with respect to the best three components normal mixture model. A Weibull distribution is also disfavored as its BIC is 572.82. We can therefore conclude that the distribution of concentration parameters of the *Planck* sample is described by a log-normal distribution, while the ME-MACS catalogue is best described by a bimodal behavior. The secondary peak at high concentration parameter in the latter distribution may be due to the CC bias, as the number of peaked objects is artificially boosted in X-ray surveys (Sec. 5.2). We tested the correlation between the concentration parameter and the dynamical indicator that we used in Paper I (i.e. the projected distance between the X-ray peak and the BCG) and found them to be significantly anti-correlated in both samples. We provide the details of this analysis in Appendix A.

4.3 Comparison with other samples in the literature

As discussed in Paper I, ME-MACS is the most suited sample to be compared with *Planck* among the well defined X-

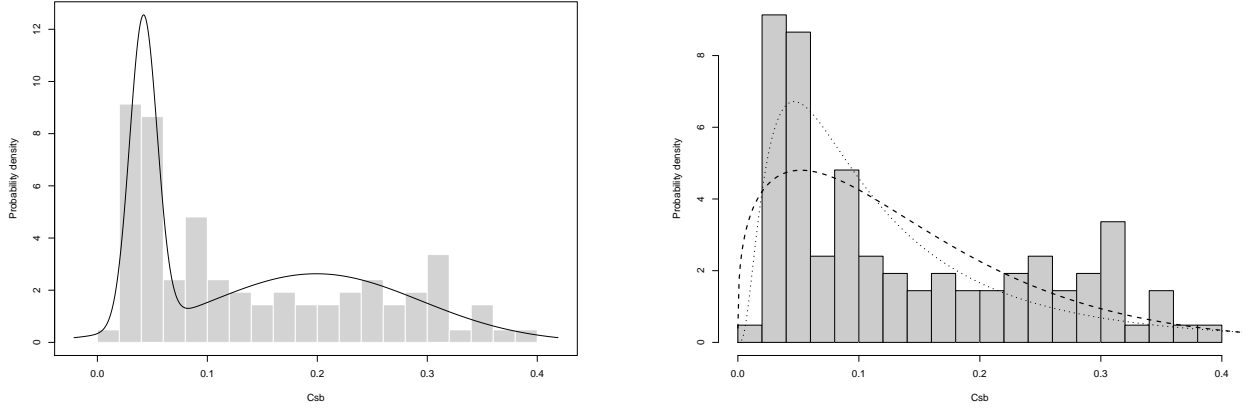


Figure 4. Left: The distribution of concentration parameters for the ME-MACS sample with the best fit two normal components model over-plotted. Right: same as in the left panel with the fit positively skewed functions: with the dotted line a log-normal and with the dashed line the Weibull function.

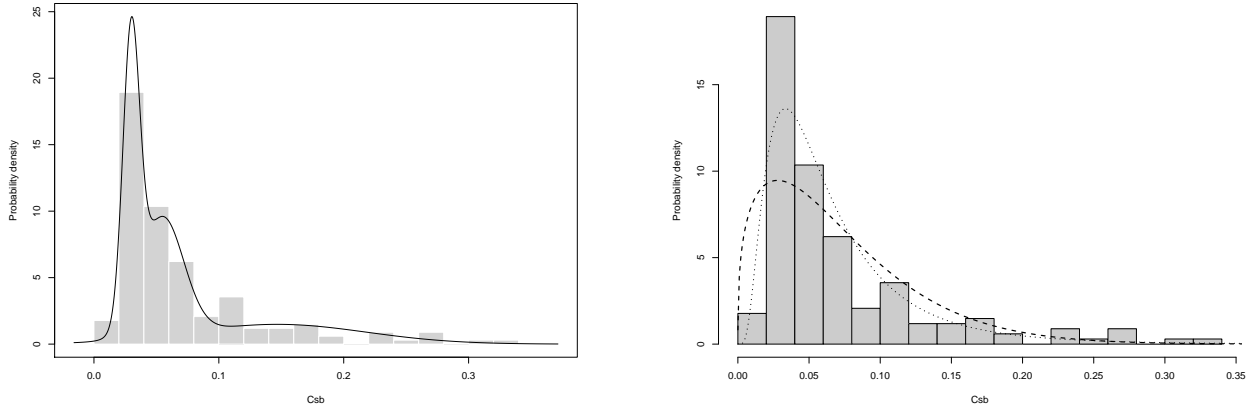


Figure 5. Left: The distribution of concentration parameters for the *Planck* sample with the best fit three normal components model over-plotted. Right: same as in the left panel with the fit positively skewed functions: with the dotted line a log-normal and with the dashed line the Weibull function.

Sample	CC fraction %	KS test $D(p_0)$	Median z	Median M_{500} $10^{14} M_{\odot}$	Number of objects
<i>Planck</i>	29 ± 4	-	0.18	6.2	169
<i>Planck</i> $z > 0.15$	29 ± 5	-	0.25	7.08	103
ME-MACS	59 ± 5	0.349 (1.7×10^{-7})	0.35	6.54	129
HIFLUGCS (X)	56 ± 6	0.316 (1.3×10^{-4})	0.047	2.70	62
V09 low- z (X)	58 ± 10	0.334 (9.0×10^{-3})	0.075	6.18	26
V09 high- z /400d (X)	31 ± 8	0.147 (5.5×10^{-1})	0.49	2.90	36
Pascut15 (X)	74 ± 5	0.471 (1.5×10^{-9})	0.50	2.72	62
Santos10 (X)	60 ± 13	0.421 (1.0×10^{-2})	0.82	2.18	15
SPT all (SZ)	29 ± 5	0.192 (3.0×10^{-2})	0.59	5.17	81
SPT low- z (SZ)	29 ± 7	0.170 (2.7×10^{-1})	0.47	5.60	41

Table 4. CC-fraction in literature samples and KS test compared with the *Planck* sample.

ray selected catalogues we used in that paper, and this is the reason we focused our analysis on it in the present paper. Nonetheless, the concentration parameter has been calculated for many other samples of galaxy clusters with the definition of Santos et al. (2008) and we can use the tabulated values for calculating their CC fraction and for doing a KS test to compare with the *Planck* sample. We found literature information on the concentration parameter for HIFLUGCS (Hudson et al. 2010, T. Reiprich private communication), the *Chandra* Deep Group survey in Pascut & Ponman (2015), a high-redshift sample computed by Santos et al. (2010) and built using WARPS (Perlman et al. 2002; Horner et al. 2008) and RDCS (Rosati et al. 1998), and the two samples used in the cosmological analysis by Vikhlinin et al. (2009): the low- z one, whose c values are provided by Santos et al. 2010, and the high- z subsample, drawn by 400d (Burenin et al. 2007), for which the c values were computed by Semler et al. (2012). We note that the the above samples span different masses and redshift ranges (as shown in Table 4) since they are derived with different limiting fluxes starting from X-ray surveys, based either on RASS (HIFLUGCS, ME-MACS) or on deep pointed PSPC observations (400d, WARPS and RDCS). We also found tabulated value of the concentration parameter for the SZ-selected SPT XVP sample, described in McDonald et al. (2013). The cool core fraction (using the same threshold value $c = 0.075$), the results of the KS test in comparison with our *Planck* sample as well as the median redshift and mass of each sample are provided in Table 4.

This analysis confirms that the ME-MACS sample is the most similar in terms of both mass and redshift to the *Planck* sample. The CC fractions of most X-ray selected samples are significantly higher than in *Planck* in all redshift and mass ranges, with the notable exception of the high-redshift sample of Vikhlinin et al. (2009), drawn from 400d, which features a fraction consistent with *Planck*. The difference between this sample and other X-ray selected samples has been already debated in the literature (e.g. Santos et al. 2010; Mantz et al. 2015) and it is beyond the scope of this paper. Nonetheless, we notice that the limiting flux of 400d (1.4×10^{-13} erg cm $^{-2}$ s $^{-1}$ Burenin et al. 2007) is higher than those of WARPS (6.5×10^{-14} erg cm $^{-2}$ s $^{-1}$) and RDCS ($1-3 \times 10^{-14}$ erg cm $^{-2}$ s $^{-1}$), also based on deep ROSAT PSPC pointed observations. Possibly, the higher flux threshold imposed in 400d with respect to the detection limit reduces the effect of the CC-bias (Eckert et al. 2011; Rosati et al. 2002) and allows to build a “representative snapshot of the cluster population of typical clusters at $z = 0.3 - 0.8$ ” (Burenin et al. 2007). We also note that the difference in the cool core fraction of RDCS+WARPS sample and 400d discussed by Santos et al. (2010) is due to the difference in limiting fluxes cited above: all the CC objects in RDCS or WARPS have a measured flux below the 400d threshold. Given that 400d is the only X-ray sample featuring a CC fraction consistent with *Planck*, it is not surprising that Semler et al. (2012) and Nurgaliev et al. (2016) found that the distribution of concentration parameters and of morphological indicators are consistent in SPT-selected samples and 400d. However, it appears clear that 400d is rather unique among X-ray samples.

The only other SZ-selected sample in Table 4 is SPT XVP (McDonald et al. 2013) which features a CC fraction con-

sistent with the one in *Planck*. Since the SPT-XVP sample extends to higher redshift (0.32–1.2) and lower masses than the *Planck* sample, we extracted a subset from the SPT catalogue in the redshift range 0.32–0.6 (41 objects) and compare it with the *Planck* sample in the same redshift range (only 24 clusters). The CC fraction are in very good agreement as SPT finds $29 \pm 7\%$, while with the *Planck* subsample we have $29 \pm 9\%$. It is certainly intriguing that both SZ-selected samples provide a similar CC fraction, but the large error bars, due to the limited number of objects in the common redshift range, do not allow us to draw strong conclusions about this agreement of the cool core fraction in different SZ-selected samples.

5 THE ROLE OF CC-BIAS

In this section, we test the hypothesis that the difference between the *Planck* and ME-MACS distributions of concentration parameters is due to the CC-bias, first by looking at the properties of clusters which are detected only in ME-MACS and not in *Planck* (Sec. 5.1) then by performing dedicated simulations (Sec. 5.2).

5.1 Missing ME-MACS clusters in *Planck*

In Fig. 1, we showed the distribution of *Planck* and ME-MACS objects in the mass-redshift plane: the mass limit of the ME-MACS sample is below the one of our *Planck* sample in the redshift range 0.2 – 0.6. Therefore, we expect to find in the *Planck* sample only the most massive ME-MACS objects, which we selected for having $M_{500} > 8 \times 10^{14} M_{\odot}$ at $z > 0.4$ or $M_{500} > 7 \times 10^{14} M_{\odot}$ in the redshift range 0.15 – 0.4. We found 36 objects in ME-MACS with the above criteria and 24 are in common with *Planck* while 12 are not found in our *Planck* sample. Of these, three are located behind the galactic mask and we are thus left with nine massive objects that should be found also in the *Planck* sample but are not. We looked at their concentration parameters and all of them are classified as cool cores. It is interesting to note that most of the “missing clusters” in our *Planck* sample feature a strongly peaked SB profile ($c > 0.2$), i.e. belong to the secondary peak of the ME-MACS distribution which is not found in the *Planck* histogram (Sec. 4.2).

We underline that the masses of ME-MACS, that we used to select potential *Planck* clusters, are calculated from the $L-M$ scaling relation (see Sec. 2.3) and may thus be biased high for CCs (e.g. Hudson et al. 2010). For 8 of the missing objects, we found independent mass measurements, either in the *Planck* catalogue (Planck Collaboration XXIX 2014) (i.e. they are detected by *Planck* with a S/N in the range 4.5–7 and thus do not enter in the cosmology sample that we analyzed here) or from weak lensing (for two of them) in the LC 2 catalogue (Sereno 2015). We show their position in the $L-M$ plane along with the common objects in the two samples in Fig. 6. Almost all the missing objects lie above the scaling relation and their independent mass measurements are below the mass limit of our *Planck* sample, explaining why they are not found in the *Planck* cosmology sample. Their luminosity (and thus their mass estimate from $L-M$) is likely boosted by the presence of the cool core.

The fact that all the objects we considered here are CC,

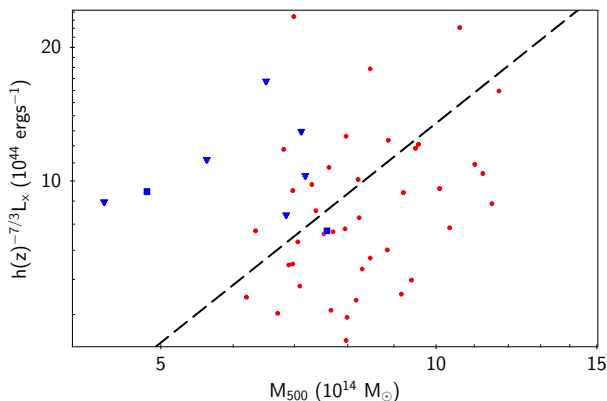


Figure 6. Distribution in the $L-M$ plane of the clusters in common between *Planck* and ME-MACS (filled red circles) and for those in ME-MACS but not in *Planck* (blue triangles for SZ-derived mass measurement and blue square for weak lensing). The dashed line marks the scaling relation of Pratt et al. (2009).

suggests that the CC-bias may have a role in explaining the difference between the two samples. However, to firmly test this hypothesis observationally, one would need to start from a complete population of clusters with independent mass measurements and to compare it with the properties of SZ-selected and X-ray selected samples with similar mass limits, to see which clusters are missing in the two samples. Unfortunately, we are not in this situation, since the ME-MACS mass limit is below the *Planck* one and the mass measurements of ME-MACS are derived from a biased quantity such as the luminosity. To firmly test the effect of CC-bias we thus need to make use of numerical simulations (Sec. 5.2).

5.2 Simulations

We performed a dedicated simulation following an approach similar to Eckert et al. (2011) and tailored to reproduce the *Planck* and ME-MACS selection criteria. The main idea of the procedure is to simulate a realistic population of clusters in the mass-redshift plane with a distribution of concentration parameters which follows the one in the *Planck* sample, apply the ME-MACS selection function to the simulated systems and measure the CC fraction in the “detected” simulated sample. We refer to Eckert et al. (2011) for the details of the simulation, here we recall the main steps and discuss the differences with respect to the previous approach.

We start by simulating a population of halos in the appropriate mass and redshift range. As opposed to Eckert et al. (2011), who started from an X-ray luminosity function tailored for their sample, here we randomly draw halos according to the mass function of Tinker et al. (2008). We then use the relation between core-excised X-ray luminosity and halo mass of Mantz et al. (2010) to calculate the expected luminosity of each halo.

To convert the core-excised luminosity into an integrated luminosity and overall flux, we associate a surface brightness profile to each simulated cluster. We underline that this is an improvement with respect to Eckert et al. (2011), because we take into account that at a fixed mass, CC clusters are actually more luminous than NCC clusters (see discussion in Hudson et al. 2010). In the original simulation, Eck-

ert et al. (2011) used a fixed surface brightness template (a beta model for NCC and a double beta model for CC) and randomly chose between the two according to a fixed input CC fraction. Here we assume that the distribution of the concentration parameters of the *Planck* sample is representative of the true distribution and we use the full measured distribution to draw a realistic distribution of surface brightness profiles. We assume that the surface brightness profile of each cluster can be approximated by a double beta model:

$$S(r) = S_1 \left(\left[1 + \left(\frac{r}{r_{c1}} \right)^2 \right]^{-3\beta+1/2} + R \left[1 + \left(\frac{r}{r_{c2}} \right)^2 \right]^{-3\beta+1/2} \right), \quad (2)$$

where the ratio between the two beta models, R , is randomly selected from a list of values that reproduce the c distribution of the *Planck* sample, while β , r_{c1} and r_{c2} are fixed to the values which best represent the observed values in the *Planck* sample ($\beta = 0.64$, $r_1 = 300$ kpc, $r_2 = 30$ kpc) and S_1 is the overall normalization, which is set on-the-fly to reproduce the core-excised luminosity of each simulated halo. This approach allows us to simulate a population spanning a whole range of surface-brightness profiles, but the results do not change significantly if a fixed template is used. After having selected a surface brightness profile, we can reproduce the integrated luminosity and the flux in the 0.1 – 2.4 keV energy range for each simulated cluster, as described in Eckert et al. (2011). A hidden assumption in this procedure is that the *Planck* distribution of concentration parameter is representative of the cluster population at all redshifts, i.e. that the CC fraction does not evolve with time, in contrast with the recent result by McDonald et al. (2013). However, this evolution becomes strongly significant only at very high redshift ($z > 0.7$), where we have very few objects both in our simulations and in the observed samples.

We then simulate the ME-MACS selection. As described in Mann & Ebeling (2012), the starting point of the ME-MACS (and also MACS, Ebeling et al. 2001) is the RASS Bright Source Catalogue (Voges et al. 1999), from which they selected candidate clusters with a flux-limit $f_{RASS} > 10^{-12}$ ergs cm $^{-2}$ s $^{-1}$. We can thus use the same procedure as in Eckert et al. (2011) to simulate the source detection as ME-MACS is a RASS-based flux-limited survey. We only apply the additional luminosity and redshift criteria in ME-MACS, namely $L_X > 5 \times 10^{44}$ ergs s $^{-1}$ and $z > 0.15$.

We run our simulation with 10^7 input halos, resulting in more than 15,000 detected clusters, for which we compute the concentration parameter. We compare the c output distribution with the input one in Fig. 7: it is apparent that a second peak of the distribution emerges at high concentration parameters (i.e. CC). While the starting population is described by the *Planck* lognormal distribution, the output of the simulation is not described by a unimodal distribution anymore and a secondary peak emerges. Our simulation thus shows that the “bimodality” (i.e. presence of two peaks) of the cluster population between CC and NCC objects, which has been largely discussed in the literature (e.g. Cavagnolo et al. 2009; Pratt et al. 2010) is at least partly due to the CC-bias.

The CC fraction in the whole simulated sample is 48%, significantly larger than the fraction in the *Planck* sample, but still lower than the measured value of the ME-MACS sample ($59 \pm 5\%$). Since the *Planck* and ME-MACS samples largely overlap and are drawn from the same underlying popula-

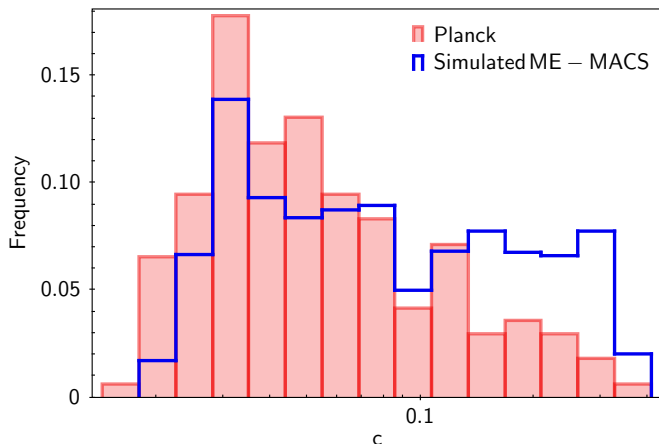


Figure 7. Distribution of the concentration parameter in the *Planck* sample (pink), used as an input in the simulation, and the output distribution of concentration parameters of the detected clusters in the ME-MACS simulation (blue). The vertical dashed line marks the threshold to separate CC ($c > 0.075$) from NCC ($c < 0.075$).

tion, there is a strong covariance between the CC fraction measured in the two samples. This covariance needs to be taken into account to assess the significance of the difference between the two samples. To this aim, we perform another set of simulations in which the number of simulated halos reproduces the expected number of halos in the redshift and mass range of interest. We then apply at the same time the *Planck* and ME-MACS selection functions to the simulated halos to draw realistic *Planck*-like and ME-MACS-like cluster samples simultaneously and calculate the CC fraction in both. To implement the *Planck* selection function, which is given as a function of the total SZ flux (Y) and the apparent opening angle (Planck Collaboration XXVII 2016), we use the $Y - M$ relation from Planck Collaboration XX (2014). We then repeat this procedure 10,000 times and compare the resulting CC bias values with the observed one. In Fig. 8 we show the 68.3% and 99.7% containment contours of the output values for the CC fraction. The figure clearly shows the strong covariance between the two measurements, which results from the fact that the two samples are not independent. In only 0.2% of the cases we are finding that the two CC fractions are consistent with the observed ones simultaneously.

To summarize, our simulation reproduces qualitatively the properties of the ME-MACS sample and the presence of two peaks. It shows that the CC-bias certainly plays a large role in the difference between the *Planck* and ME-MACS distribution, but at the same time suggests that is unlikely that CC-bias alone can account for the full difference. However we should remind that our attempt to reproduce the effect of the CC bias, although sophisticated, is based on several assumptions and, as any simulation, cannot fully reproduce the complexity of the clusters population and of the X-ray and SZ selection. Moreover, as our samples are not fully complete, there is still the possibility that the difference may be fully explained by the CC bias, if we assume that the 12 missing clusters in the *Planck* $z > 0.15$ sample (Sec. 2.1) are CC (rising the CC fraction to 36%) and all unobserved

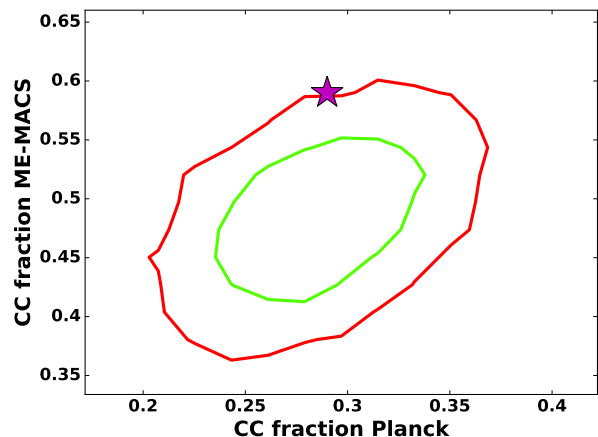


Figure 8. Probability contours of the CC fraction drawn from 10,000 simulated populations of massive clusters, applying the *Planck* and ME-MACS selection functions to the simulated data. The contours represent a containment of 68.3% (red) and 99.7% (green) of the simulations. The magenta star shows the true *Planck* and ME-MACS CC fractions.

objects in ME-MACS (25, Sec. 2.2) are NCC (lowering it to 47%). Although we consider this hypothesis unlikely, we cannot exclude it given the incompleteness of our sample.

6 BEYOND THE CC BIAS

In Sec. 5, we focused our attention on the role of CC-bias in explaining the difference between the *Planck* and ME-MACS distribution. However, there are other mechanisms, both in the SZ and in the X-ray selection, that can contribute to the difference and that can be highlighted by the comparison of our samples. In this Section, we will discuss the role of possible biases against CCs in the *Planck* survey (Sec. 6.1) and the effect due to a population of X-ray underluminous objects (Sec. 6.2) in the *Planck* catalogue (Planck Collaboration XXVII 2016).

6.1 An anti-CC bias in the *Planck* SZ survey

It has been suggested that the presence of bright radio galaxies at the centres of CC clusters may induce a bias against CCs in SZ surveys, since radio-sources could potentially influence the cluster detection and measurement of the SZ signal (e.g. Sayers et al. 2013a; Lin et al. 2015) and are thus usually masked out in the SZ analysis. As discussed in Planck Collaboration XXIX (2014), this bias is expected to be small in the *Planck* survey, as the cluster detection is performed with HFI at high frequencies, where the emission of steep-spectrum radio sources is negligible with respect to the SZ effect. Nonetheless, we tried to estimate this possible bias which could in principle contribute to the residual difference that we found in Sec. 5.2. The point source mask used in the *Planck* analysis was built starting from the *Planck* compact source catalogues (PCCS, Planck Collaboration XXVIII, 2014) at several frequencies, excluding a circle of radius 2.13 FWHM around point sources detected with signal-to-noise ratio larger than ten (Planck Collaboration XXIX 2014). Starting from

the Meta-Catalogue of X-ray detected Clusters (MCXC, Piffaretti et al. 2011), we looked for known clusters whose position is within a radius of 2.13 FWHM around bright point sources in at least one out of the six HFI frequencies, finding 57 candidate “missing” clusters. However, most of these objects have low masses and should not be detectable by *Planck*. Only for 6 objects (namely Perseus, Cygnus A, Abell 780, RXC J1130.3 – 1434, RXC J1025.9 + 1241, Abell S1111) the masses in the MCXC catalogue are comparable with the masses of clusters in the PSZ1-cosmo sample at the same redshift and they could thus be detected in the survey if they were not behind the mask. Perseus, Cygnus-A and Abell 780 are well known CC clusters, while we could not find any literature information about the core state of the remaining three objects, whose expected mass is furthermore close to the limit of the selection function in the mass-redshift plane and may thus be not detected by *Planck*, also for statistical reasons. We can thus roughly estimate that the *Planck* catalogue is missing 3-6 objects because of radio sources, and assuming that they are all CC, the corrected CC fraction would be 30 – 31%. The bias due to radio-galaxies in CC is thus only 1 – 2%, smaller than the statistical error on the CC fraction in the *Planck* sample, and not sufficient to reach the CC fraction of 38% that would be needed to reproduce the ME-MACS fraction with our simulation of the CC bias.

Another possible reason for which the *Planck* SZ survey may be biased against CC is that through the SZ effect we may in principle detect more easily disturbed merging clusters, where the SZ signal may be enhanced by shock fronts propagating in the ICM. Indeed, Sommer & Basu (2014) showed that the SZ signal within R_{500} in simulated clusters is boosted after a merger on a time-scale of a few Gyr. The selection function and its dependence on the dynamical state of the *Planck* SZ survey has been tested in Planck Collaboration XXVII (2016) with Monte-Carlo simulations, by injecting simulated clusters with different y maps in the *Planck* sky maps and running the detection algorithms, showing that the cluster morphology does not impact significantly the source detection. This result is not unexpected if we take into account the large beams of the *Planck* frequency channels: similarly to what happens to the peaked pressure profile of CC clusters, over-pressurized regions due to shocks are smoothed out by the *Planck* moderate spatial resolution. Moreover, *Planck* is more sensitive to the behaviour of the pressure profiles at large scales than to the smaller-scale physics (such as cool cores or shock) and it measures the SZ signal on scales larger than R_{500} (i.e. the region studied by Sommer & Basu 2014). Recently, Nurgaliev et al. (2016) suggested that *Planck* may be more sensitive to pairs or triplets of galaxy clusters, because of its large beam capturing an inflated signal from multiple objects and therefore may be biased towards merging systems. While it is certainly true that *Planck* has detected a few of these objects that received a lot of attention in the literature (Planck Collaboration, IX, 2011; Planck Collaboration, VI, 2013), in the high purity PSZ1 cosmology sample that we analyzed in this paper and in Paper I, we do not have a large number of these objects. Moreover, clusters in multiple systems are not necessarily disturbed NCC objects: for instance, the brightest member in the *Planck* discovered supercluster PLCK G214.6 + 37.0

features a prominent surface brightness peak associated to the BCG (Planck Collaboration, VI, 2013), which would led us to classify it as a CC relaxed object.

Last but not least, if there were a systematic difference between the pressure profile of CC and NCC clusters at $R \gtrsim R_{500}$, with NCC clusters showing flatter profile than CC clusters similarly to what observed in the gas density distribution (Eckert et al. 2012), NCC could possibly have a larger SZ signal at large scales making them easier to detect in SZ. However, the analysis of the pressure profiles of samples of galaxy clusters both with *Planck* (Planck Collaboration, V, 2013) and with Bolocam (Sayers et al. 2013b) show only a moderate difference at large scales and with a large dispersion. Indeed, if we assume the best fit models for CC and NCC objects in the analysis of *Planck* pressure profiles (Planck Collaboration, V, 2013) and we integrate them to measure the SZ signal at $5R_{500}$, the derived values differ only by 2%. Nonetheless, the SZ flux at $5R_{500}$ depends strongly on the shape of the pressure profile: if we assume a combination of parameters consistent at 68% with the best fit model but with a flatter outer slope $\beta = 3.2$ (basing on Fig. 5 in Planck Collaboration, V, 2013), the derived $Y_{5R_{500}}$ would be 12% larger than the value with the mean CC profile. We underline that the sample of clusters for which the *Planck* pressure profile has been measured is not SZ-selected, as it is composed of early *Planck* detections already known in X-rays and with available *XMM-Newton* data (Planck Collaboration, V, 2013), thus the derived pressure profile may not be representative of the cluster population. While present data do not allow to provide support to the hypothesis of an anti-CC bias in *Planck* more detailed studies on larger and well-defined samples are needed to reduce the uncertainties and to firmly assess the shape of the CC and NCC pressure profiles and their role on the SZ detection procedures.

6.2 X-ray underluminous clusters

One unexpected result of the *Planck* SZ survey has been the discovery of a population of X-ray under-luminous clusters (Planck Collaboration XXVII 2016). These systems feature an X-ray luminosity which is well below the value that could be expected through scaling relations from the SZ signal, while their optical richness is in agreement with expectations. This population was highlighted at low redshift and in the SDSS sky area, but it possibly extends also to other redshift ranges and sky regions. If this population exists also in our *Planck* sample and if all, or most, under-luminous clusters are classified as NCC, it could contribute in explaining the difference between the CC fraction in the *Planck* sample and in ME-MACS. **As these objects by definition obey to a different $L - M$ scaling relation than the one we used in Sec. 5.2, their presence is not accounted for in our simulation.**

One method to highlight this population in our *Planck* sample is to look at the clusters which should have been detected also in ME-MACS but are not (complementary to what we showed in 5.1). We thus select all clusters in the *Planck* sample which lie in the sky region covered by ME-MACS, have $z > 0.15$ and an expected luminosity larger than the ME-MACS threshold (see Mann & Ebeling 2012 for details) but

are missing in the ME-MACS sample. To estimate the expected luminosity, we convert the SZ signal Y_{500} in the *Planck* catalogue into L_{500} , using the $L_{500} - Y_{500}$ relation obtained in [Planck Collaboration XXVII \(2016\)](#). With this method, we find 24 missing clusters in ME-MACS, most of which (19) are NCC objects. In Fig. 9, we compare their measured luminosity³ L_{500} as a function of their SZ signal, with the scaling relation and its scatter, calibrated on *Planck* clusters by [Planck Collaboration XXVII \(2016\)](#). We notice that almost all objects lie below the expected relation and some of them below twice the intrinsic scatter, which would lead to their classification as “underluminous” objects, following [Planck Collaboration XXVII \(2016\)](#). According to the concentration parameter, all the most deviating objects are classified as NCC. We noticed that in a few cases the measured luminosity is above the selection threshold of the ME-MACS sample (5×10^{44} ergs s⁻¹). However, we used luminosities within R_{500} , while the luminosity used in the selection of the ME-MACS sample is estimated in the RASS detection cell. Indeed, one of the most luminous clusters in Fig. 9 is A115N, which has $L_{500} = 7.5 \times 10^{44}$ ergs s⁻¹ in MCXC, but with $L_{RASS, det} = 4.4 \times 10^{44}$ ergs s⁻¹ it fails to make the luminosity cut in ME-MACS (H. Ebeling, private communication). The population of X-ray under-luminous clusters is thus likely present also in the *Planck* sample we are analyzing. It is intriguing that candidate X-ray underluminous clusters in our sample are almost all classified as NCC: if this population, which is missing in X-ray surveys but is detected in SZ, is composed of disturbed NCC clusters, they could certainly contribute to the residual difference between the *Planck* and ME-MACS distribution of concentration parameters. At the moment, little is known about these objects, and it is unclear if they are truly X-ray underluminous for their mass or if their SZ signal is artificially boosted. New observations, both in X-rays and possibly in SZ, are needed to assess the origin of this class of objects. A systematic analysis of their properties and the cool-core state of X-ray under-luminous clusters is beyond the scope of this paper and will be presented in a forthcoming work with new dedicated data (Rossetti et al. in prep.).

7 SUMMARY AND CONCLUSIONS

In this paper, we studied the cool core state of a SZ-selected sample of galaxy clusters, the cosmological sample of the first *Planck* SZ catalogue ([Planck Collaboration XXIX 2014](#)), using as indicator the concentration parameter ([Santos et al. 2008](#)). Our results are summarized as follows.

- The distribution of the concentration parameters in the *Planck* sample features a single peak at low values of c . The fraction of CC clusters ($c > 0.075$) is $(29 \pm 4)\%$.
- We do not find indications of evolution of the CC fraction by dividing our sample in two redshift bins. Our result does not contradict previous detections which report evolution in a redshift range ($z > 0.3$) which is poorly sampled

³ For most objects, we used the luminosity in the MCXC catalogue ([Piffaretti et al. 2011](#)), while for 5 objects we measured the luminosity directly from the *Chandra* data.

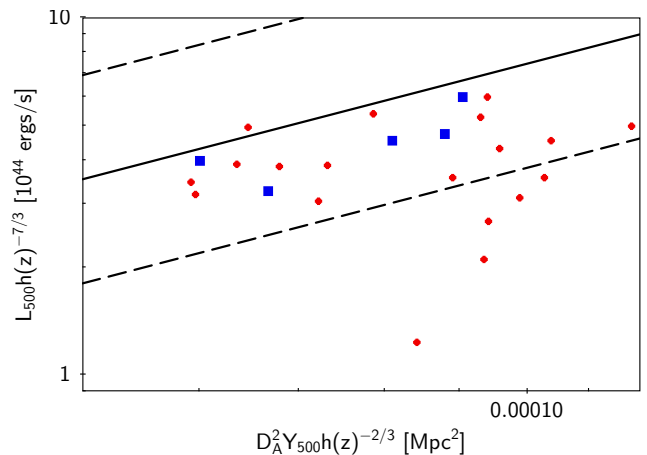


Figure 9. Distribution in the $Y_{500} - L_{500}$ plane of the 24 missing ME-MACS clusters, compared with the best-fit scaling relation (black continuous line) and its dispersion ($\pm 2\sigma$, dashed lines) estimated in [Planck Collaboration XXVII \(2016\)](#). We mark with blue squares CC clusters and with red points NCC.

by our catalogue ([McDonald et al. 2013](#)). We find an indication of a larger CC fraction in higher mass systems, as reported also in [Mantz et al. \(2015\)](#), but only at low significance (1.5σ).

- We compared the distribution of the concentration parameter with the one of the X-ray selected ME-MACS sample ([Mann & Ebeling 2012](#)). The distributions are significantly different with a 1.7×10^{-7} probability that they are drawn from the same population of objects. Indeed, ME-MACS hosts a much larger fraction of CC objects: $(59 \pm 5)\%$.

• The distributions of concentration parameters in ME-MACS shows two peaks and is well described by two Gaussians. This double peaked distribution, which is observed also in other X-ray selected samples and with other cool-core indicator ([Cavagnolo et al. 2009](#); [Pratt et al. 2010](#)) has opened a debate in the literature whereas the cluster population is bimodal or not. However, our *Planck* sample is better described by a single lognormal distribution. We showed with simulations that a secondary peak at high concentration parameters emerges in X-ray flux-limited samples as a consequence of the CC-bias and the presence of two peaks may thus not be an intrinsic property of the cluster population.

- Among the X-ray selected samples available in the literature, ME-MACS is the one with the mass and redshift distributions more similar to the *Planck* sample ([Rossetti et al. 2016](#)). Nonetheless, we compared the c distribution in *Planck* with the one of other X-ray samples and found them to be significantly different, having CC fractions in the range 56 – 74%. We also compared our distribution with the one in the SZ selected sample of SPT clusters ([McDonald et al. 2013](#)), finding them to be consistent with a comparable CC fraction ($29 \pm 7\%$) in the common redshift range.

• A possible origin of the discrepancy between the CC fraction in SZ-selected and X-ray selected samples is the CC-bias ([Eckert et al. 2011](#)). We tested this hypothesis with simulations of the CC bias: starting from a realistic population of clusters with the distribution of concentration parameters in the *Planck* sample, we simulate the ME-MACS

selection and measure the CC fraction in the output sample (Sec. 5.2). Starting from a CC-fraction of 29% in the input population, we obtain a CC fraction of 48% in the output sample, showing that CC-bias plays a large role in the difference between the two samples. Nonetheless, according to our simulation, the probability of obtaining simultaneously two CC-fractions of 29% in *Planck* and 59% in ME-MACS is only 0.2%.

- We considered several mechanisms that could also possibly affect SZ surveys to be biased against CC, namely the presence of radio galaxies in CCs, the role of shocks in increasing the SZ signal, the large *Planck* beam favoring the detection of multiple disturbed objects and a difference in the pressure profile at large radii. However, none of them seem sufficient to explain the difference between the observed CC-fraction in ME-MACS and the one in *Planck*.

- We noticed that the *Planck* sample host a population of objects, which according to their expected luminosity (from $L - Y$ scaling relation) should be present also in ME-MACS, but are not since their observed luminosity is below the luminosity cut in that sample. Most of these X-ray underluminous objects are classified as NCC. The presence of this population of clusters, whose origin and properties are still unclear, in the *Planck* sample could possibly contribute to the difference.

ACKNOWLEDGEMENTS

We dedicate this paper to the memory of our colleague Y.Y. Zhang: we are indebted to her work [Zhang et al. \(2011\)](#) for the analysis discussed in Paper I, on which the present paper is based. We thank H. Ebeling for useful information about the ME-MACS sample and T. Reiprich for providing the concentration parameters of HIFLUGCS clusters.

REFERENCES

- Arnaud M., Pointecouteau E., Pratt G. W., 2005, [A&A](#), **441**, 893
- Battaglia N., Bond J. R., Pfrommer C., Sievers J. L., 2012, [ApJ](#), **758**, 74
- Bleem L. E., et al., 2015, [ApJS](#), **216**, 27
- Böhringer H., et al., 2000, [ApJS](#), **129**, 435
- Böhringer H., et al., 2004, [A&A](#), **425**, 367
- Böhringer H., et al., 2007, [A&A](#), **469**, 363
- Burenin R. A., Vikhlinin A., Hornstrup A., Ebeling H., Quintana H., Mescheryakov A., 2007, [ApJS](#), **172**, 561
- Cavagnolo K. W., Donahue M., Voit G. M., Sun M., 2009, [ApJS](#), **182**, 12
- Chen Y., Reiprich T. H., Böhringer H., Ikebe Y., Zhang Y.-Y., 2007, [A&A](#), **466**, 805
- David L. P., Kempner J., 2004, [ApJ](#), **613**, 831
- Ebeling H., Edge A. C., Henry J. P., 2001, [ApJ](#), **553**, 668
- Eckert D., Molendi S., Paltani S., 2011, [A&A](#), **526**, A79
- Eckert D., et al., 2012, [A&A](#), **541**, A57
- Fakhouri O., Ma C.-P., Boylan-Kolchin M., 2010, [MNRAS](#), **406**, 2267
- Finoguenov A., Henriksen M. J., Miniati F., Briel U. G., Jones C., 2006, [ApJ](#), **643**, 790
- Fraley C., Raftery A. E., 2002, Journal of the American Statistical Association, **97**, 611
- Fraley C., Raftery A. E., Murphy T. B., Scrucca L., 2012, mclust Version 4 for R: Normal Mixture Modeling for Model-Based Clustering, Classification, and Density Estimation
- Girardi M., Boschin W., Barrena R., 2006, [A&A](#), **455**, 45
- Hasselfield M., et al., 2013, [J. Cosmology Astropart. Phys.](#), **7**, 8
- Horner D. J., Perlman E. S., Ebeling H., Jones L. R., Scharf C. A., Wegner G., Malkan M., Maughan B., 2008, [ApJS](#), **176**, 374
- Hudson D. S., Mittal R., Reiprich T. H., Nulsen P. E. J., Andernach H., Sarazin C. L., 2010, [A&A](#), **513**, A37
- Kass R. E., Raftery A. E., 1995, Journal of the American Statistical Association, **90**, 773
- Krause E., Pierpaoli E., Dolag K., Borgani S., 2012, [MNRAS](#), **419**, 1766
- Lin H. W., McDonald M., Benson B., Miller E., 2015, [ApJ](#), **802**, 34
- Mann A. W., Ebeling H., 2012, [MNRAS](#), **420**, 2120
- Mantz A., Allen S. W., Ebeling H., Rapetti D., Drlica-Wagner A., 2010, [MNRAS](#), **406**, 1773
- Mantz A. B., Allen S. W., Morris R. G., Schmidt R. W., von der Linden A., Urban O., 2015, [MNRAS](#), **449**, 199
- McDonald M., Benson B. A., Vikhlinin A., Stalder B., Bleem L. E., de Haan T., Lin H. W., Aird K. A., 2013, [ApJ](#), **774**, 23
- Menanteau F., et al., 2012, [ApJ](#), **748**, 7
- Motl P. M., Hallman E. J., Burns J. O., Norman M. L., 2005, [ApJ](#), **623**, L63
- Nurgaliev D., et al., 2016, submitted to [ApJ](#), astro-ph:1609.00375,
- Pascut A., Ponman T. J., 2015, [MNRAS](#), **447**, 3723
- Perlman E. S., Horner D. J., Jones L. R., Scharf C. A., Ebeling H., Wegner G., Malkan M., 2002, [ApJS](#), **140**, 265
- Pesce J. E., Fabian A. C., Edge A. C., Johnstone R. M., 1990, [MNRAS](#), **244**, 58
- Pierre M., et al., 2016, [A&A](#), **592**, A1
- Piffaretti R., Arnaud M., Pratt G. W., Pointecouteau E., Melin J.-B., 2011, [A&A](#), **534**, A109
- Pipino A., Pierpaoli E., 2010, [MNRAS](#), **404**, 1603
- Planck Collaboration, IX, 2011, [A&A](#), **536**, A9
- Planck Collaboration, V, 2013, [A&A](#), **550**, A131
- Planck Collaboration, VI, 2013, [A&A](#), **550**, A132
- Planck Collaboration, VIII, 2011, [A&A](#), **536**, A8
- Planck Collaboration XX 2014, [A&A](#), **571**, A20
- Planck Collaboration XXIX 2014, [A&A](#), **571**, A29
- Planck Collaboration XXVII 2016, [A&A](#), **594**, A27
- Planck Collaboration, XXVIII, 2014, [A&A](#), **571**, A28
- Pratt G. W., Croston J. H., Arnaud M., Böhringer H., 2009, [A&A](#), **498**, 361
- Pratt G. W., et al., 2010, [A&A](#), **511**, A85
- R Core Team 2015, R: A Language and Environment for Statistical Computing. R Foundation for Statistical Computing, Vienna, Austria, <https://www.R-project.org>
- Raftery A., 1995, Bayesian Model Selection in Social Research
- Reiprich T. H., Böhringer H., 2002, [ApJ](#), **567**, 716
- Rosati P., Della Ceca R., Norman C., Giacconi R., 1998, [ApJ](#), **492**, L21
- Rosati P., Borgani S., Norman C., 2002, [ARA&A](#), **40**, 539
- Rossetti M., Molendi S., 2010, [A&A](#), **510**, A83
- Rossetti M., et al., 2016, [MNRAS](#), **457**, 4515
- Sanderson A. J. R., Edge A. C., Smith G. P., 2009, [MNRAS](#), **398**, 1698
- Santos J. S., Rosati P., Tozzi P., Böhringer H., Ettori S., Binamini A., 2008, [A&A](#), **483**, 35
- Santos J. S., Tozzi P., Rosati P., Böhringer H., 2010, [A&A](#), **521**, A64
- Sayers J., et al., 2013a, [ApJ](#), **764**, 152
- Sayers J., et al., 2013b, [ApJ](#), **768**, 177
- Schwarz G., 1978, [Ann. Stat.](#), **6**, 461
- Semler D. R., et al., 2012, [ApJ](#), **761**, 183
- Sereno M., 2015, [MNRAS](#), **450**, 3665
- Snowden S. L., Mushotzky R. F., Kuntz K. D., Davis D. S., 2008, [A&A](#), **478**, 615
- Sommer M. W., Basu K., 2014, [MNRAS](#), **437**, 2163

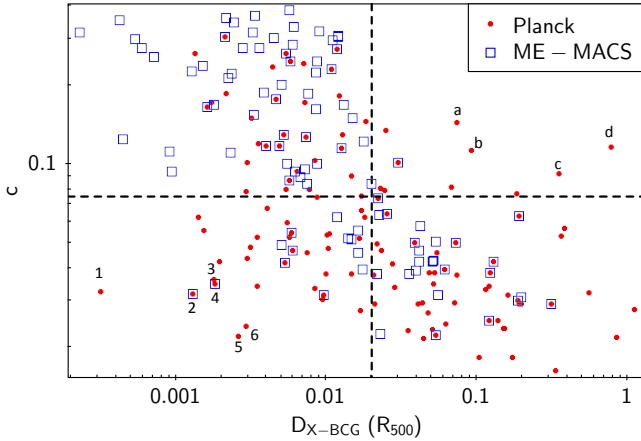


Figure A1. Distribution in the $D_{X-BCG} - c$ plane of *Planck* (red circles) and ME-MACS (blue open squares) clusters. Dashed lines mark the separation between CC/NCC and relaxed/disturbed clusters. Objects in the upper left quadrant are relaxed CC while in the lower quadrant lie disturbed NCC systems.

- Sunyaev R. A., Zeldovich Y. B., 1970, *Comments on Astrophysics and Space Physics*, **2**, 66
- Sunyaev R. A., Zeldovich Y. B., 1972, *Comments on Astrophysics and Space Physics*, **4**, 173
- Tinker J., Kravtsov A. V., Klypin A., Abazajian K., Warren M., Yepes G., Gottlöber S., Holz D. E., 2008, *ApJ*, **688**, 709
- Venables W. N., Ripley B. D., 2002, *Modern Applied Statistics with S*, fourth edn. Springer, New York, <http://www.stats.ox.ac.uk/pub/MASS4>
- Vikhlinin A., et al., 2009, *ApJ*, **692**, 1060
- Voges W., et al., 1999, *A&A*, **349**, 389
- Zhang Y.-Y., Andernach H., Caretta C. A., Reiprich T. H., Böhringer H., Puchwein E., Sijacki D., Girardi M., 2011, *A&A*, **526**, A105

APPENDIX A: CORRELATION WITH D_{X-BCG}

As discussed in Sec. 1, the concentration parameter is an indicator of the presence of a CC, while the indicator used in Paper I, i.e. D_{X-BCG} the projected distance between the X-ray peak and the BCG, is an indicator of dynamical activity. CC are usually found in dynamically relaxed systems and D_{X-BCG} has been shown to correlate with thermodynamical indicators of the cool core state (Sanderson et al. 2009). Here, we test the correlation between D_{X-BCG} and c for the *Planck* and ME-MACS sample. For *Planck* we used the values in Paper I for the 122 common clusters, while for ME-MACS we used the values provided for the full sample in Mann & Ebeling (2012). The correlation plot is shown in Fig. A1, where we also show the threshold values that we used to classify clusters in CC/NCC here and relaxed/disturbed in Paper I ($D_{X-BCG} = 0.02R_{500}$). We performed the Spearman and Kendall correlations test on both samples separately and on the joint sample. The results are shown in Table A1. In both datasets separately and in the joint one we find a significant anti correlation between the two indicators, with most relaxed clusters being also CC and disturbed ones be-

Sample	Spearman ρ	p_0	Kendall τ	p_0
<i>Planck</i>	-0.43	$6 \cdot 10^{-7}$	-0.30	$8 \cdot 10^{-7}$
ME-MACS	-0.74	$2 \cdot 10^{-19}$	-0.54	$4 \cdot 10^{-16}$
Joint	-0.60	$2 \cdot 10^{-23}$	-0.43	-

Table A1. Output of correlation tests

ing NCC. The correlation is stronger for ME-MACS than for *Planck* which hosts a larger number of outliers, i.e. clusters classified as relaxed but without a CC (possibly for projection effects) and disturbed objects with a CC. We investigated one by one the most outstanding outliers in the plot, that we label with numbers and letters in Fig. A1, with the aim of trying to understand if their presence in *Planck* but not in ME-MACS may be related to selection effects. The lower left quadrant of the plot contains clusters classified as “relaxed NCC”: as discussed in Paper I, we expect that 7.5% of the clusters classified as relaxed by D_{X-BCG} are in fact disturbed objects where the separation between the X-ray peak and the BCG occurs mainly along the line of sight. Moreover an intrinsic limitation of the dynamical indicator D_{X-BCG} is that not all mergers, and not all phases of the mergers, cause an offset between the BCG and the X-ray peak. The most deviating outliers in this panel are: (1) A2147 (Hudson et al. 2010, $z = 0.03$), (2) A1758N (David & Kempner 2004, $z = 0.27$, also in ME-MACS), (3) A3266 (Finoguenov et al. 2006, $z = 0.05$), (4) A697 (Girardi et al. 2006, $z = 0.28$, also in ME-MACS), (5) A119 (Hudson et al. 2010, $z = 0.05$), and (6) A1437 ($z = 0.13$, little X-ray information is available in the literature, our own analysis shows a disturbed and elongated morphology). Visual inspection of their X-ray images shows that they are all clearly disturbed objects undergoing mergers, as also supported by the literature. Most of them are simply not in ME-MACS because they are local systems ($z < 0.15$), while the only two objects at $z > 0.15$ are also found in ME-MACS.

The upper right panels contains object classified as “disturbed CC” and is populated mainly by *Planck* objects. The most deviating objects are: (a) RXC J0232.2-4420 (see image in the ACCEPT archive Cavagnolo et al. 2009, $z = 0.28$), (b) RXC J0638.7-5358 (see image in the ACCEPT archive Cavagnolo et al. 2009, $z = 0.22$), (c) SPT-CL J0411-4819 (McDonald et al. 2013, $z = 0.43$) and (d) ACT-CL J0102-4915 a.k.a. El Gordo (Menanteau et al. 2012, $z = 0.89$). It is interesting to note that all these clusters feature a significant surface brightness peak in an overall disturbed X-ray morphology. El Gordo is probably the most striking example: Menanteau et al. (2012) show that it is undergoing a major merger but it preserves a bright region with cool, low entropy and high metal abundance gas, likely the “cool core remnant” (Rossetti & Molendi 2010) of one of the merging substructures. Similar systems should be in principle easily detected also in X-ray surveys: however they are not in ME-MACS simply because they do not fall in the sky area surveyed by MACS ($\delta > -40$, Mann & Ebeling 2012).

Analysis of the outliers in this relation could have been in principle very useful to suggest possible selection effects but we are unfortunately limited by the incomplete spatial and redshift overlap of the two surveys, as discussed also in Sec. 5.1.

INDEX	NAME	Alt. Name	R.A. _x	Dec. _x	Redshift	M_{500} $10^{14}M_{\odot}$	c	σ_c	Obs. ID
6	PSZ1 G002.77-56.16	RXC J2218.6-3853	22:18:39.66	-38:53:59.0	0.141	4.4	0.0585	0.0032	15101
10	PSZ1 G003.93-59.42	RXC J2234.5-3744	22:34:27.53	-37:43:57.0	0.150	6.6	0.0332	0.0016	15303
17	PSZ1 G006.45+50.56	RXC J1510.9+0543	15:10:56.09	+05:44:40.8	0.076	6.8	0.1701	0.0019	6101
18	PSZ1 G006.68-35.52	RXC J2034.7-3548	20:34:48.74	-35:50:54.6	0.089	4.0	0.0216	0.0017	12274
23	PSZ1 G008.33-64.74	ACO S 1077	22:58:48.32	-34:47:59.1	0.312	7.7	0.0478	0.0019	1562
24	PSZ1 G008.42-56.34	RXC J2217.7-3543	22:17:45.55	-35:43:22.4	0.148	4.8	0.0927	0.0050	15116
26	PSZ1 G009.02-81.22	RXC J0014.3-3023	00:14:19.04	-30:23:30.0	0.306	9.5	0.0223	0.0009	2212,7915,8477,8557
54	PSZ1 G021.10+33.24	RXC J1632.7+0534	16:32:46.94	+05:34:32.1	0.151	7.9	0.3035	0.0013	499,6104,7940
74	PSZ1 G028.77-33.56	RXC J2048.1-1750	20:48:10.80	-17:51:21.6	0.147	4.7	0.0189	0.0011	0654440401
76	PSZ1 G029.10+44.54	RXC J1602.3+1601	16:02:16.32	+15:58:12.0	0.035	2.9	0.0325	0.0007	0505210601
92	PSZ1 G033.43-48.44	RXC J2152.4-1933	21:52:21.26	-19:32:52.1	0.094	4.1	0.1446	0.0028	4202
93	PSZ1 G033.84+77.17	RXC J1348.8+2635	13:48:52.54	+26:35:32.0	0.062	4.5	0.1810	0.0007	10898,10899,12026,18424,5289,5290
94	PSZ1 G034.03-76.59	RXC J2351.6-2605	23:51:39.36	-26:05:01.9	0.226	6.8	0.1642	0.0041	2214
108	PSZ1 G039.81-39.96	RXC J2127.1-1209	21:27:09.13	-12:10:03.0	0.175	5.7	0.0183	0.0018	15103,16292
113	PSZ1 G040.63+77.13	RXC J1349.3+2806	13:49:23.84	+28:06:32.1	0.074	3.2	0.0753	0.0046	15153
120	PSZ1 G042.85+56.63	RXC J1522.4+2742	15:22:29.42	+27:42:20.23	0.072	4.3	0.0794	0.0010	3182
122	PSZ1 G044.24+48.66	RXC J1558.3+2713	15:58:20.88	+27:13:44.2	0.089	8.8	0.0802	0.0003	1196,1228,15186,16564,16565,5005
125	PSZ1 G044.77-51.30	RXC J2214.9-1400	22:14:57.28	-14:00:12.9	0.502	8.4	0.0666	0.0043	3259,5011
137	PSZ1 G046.09+27.16	RXC J1731.6+2251	17:31:39.64	+22:52:11.1	0.388	7.9	0.0187	0.0034	3281
140	PSZ1 G046.48-49.42	RXC J2210.3-1210	22:10:18.98	-12:09:50.5	0.084	4.4	0.0341	0.0020	8271
141	PSZ1 G046.90+56.48	RXC J1524.1+2955	15:24:07.53	+29:53:16.8	0.114	5.4	0.0217	0.0011	4965
153	PSZ1 G049.22+30.84	RXC J1720.1+2637	17:20:10.52	+26:37:47.0	0.164	6.3	0.1258	0.0022	4361
164	PSZ1 G053.42-36.25	RXC J2135.2-0102	21:35:11.05	-01:02:53.2	0.330	7.5	0.0386	0.0030	11710,16285
166	PSZ1 G053.52+59.52	RXC J1510.1+3330	15:10:13.36	+33:30:39.5	0.112	4.9	0.0314	0.0004	12885,12886,13192,13193,2204
174	PSZ1 G055.58+31.87	RXC J1722.4+3208	17:22:27.32	+32:07:57.4	0.224	7.3	0.1167	0.0031	5007
177	PSZ1 G055.95-34.87	RXC J2135.2+0125	21:35:18.29	+01:25:27.8	0.231	6.9	0.0296	0.0035	15097
180	PSZ1 G056.79+36.30	RXC J1702.7+3403	17:02:42.72	+34:03:40.4	0.095	4.0	0.1010	0.0009	4179
181	PSZ1 G056.94-55.06	RXC J2243.3-0935	22:43:21.19	-09:35:37.2	0.446	10.	0.0252	0.0033	3260
183	PSZ1 G057.28-45.37	RXC J2211.7-0349	22:11:45.87	-03:49:47.3	0.397	9.2	0.1006	0.0042	3284
185	PSZ1 G057.63+34.92	RXC J1709.8+3426	17:09:49.15	+34:27:11.3	0.080	3.6	0.0233	0.0021	12284
224	PSZ1 G067.19+67.44	RXC J1426.0+3749	14:26:03.12	+37:49:24.9	0.171	6.9	0.0632	0.0014	3593,542
238	PSZ1 G071.63+29.78	RXC J1747.2+4512	17:47:08.99	+45:12:44.9	0.156	4.3	0.0207	0.0028	15118
242	PSZ1 G072.61+41.47	RXC J1640.3+4642	16:40:19.94	+46:42:45.3	0.228	11.	0.0316	0.0008	896
248	PSZ1 G073.98-27.83	RXC J2153.5+1741	21:53:36.81	+17:41:43.1	0.232	9.4	0.1287	0.0011	4193
252	PSZ1 G075.71+13.51	RXC J1921.1+4357	19:21:10.90	+43:56:45.4	0.055	8.5	0.0466	0.0003	15187,3231
256	PSZ1 G077.89-26.62	RXC J2200.8+2058	22:00:52.51	+20:58:04.9	0.146	5.4	0.0677	0.0033	3247
268	PSZ1 G081.01-50.92	RXC J2311.5+0338	23:11:33.25	+03:38:08.2	0.299	7.5	0.0644	0.0032	11730,3288
291	PSZ1 G085.98+26.69	RXC J1819.9+5710	18:19:54.00	+57:09:21.4	0.179	4.2	0.0279	0.0036	15131,16579
297	PSZ1 G087.03-57.37	RXC J2337.6+0016	23:37:37.92	+00:16:03.3	0.277	6.9	0.0302	0.0024	11728,3248
313	PSZ1 G091.82+26.11		18:31:08.59	+62:14:12.96	0.822	7.4	0.0344	0.0067	18285
319	PSZ1 G092.67+73.44	RXC J1335.3+4059	13:35:16.29	+41:00:00.4	0.227	8.2	0.0384	0.0025	3591
325	PSZ1 G093.93+34.92	RXC J1712.7+6403	17:12:39.96	+64:03:16.8	0.080	5.1	0.0184	0.0005	894
341	PSZ1 G097.72+38.13	RXC J1635.8+6612	16:35:51.25	+66:12:36.5	0.170	6.4	0.0417	0.0014	1454,1666,553
388	PSZ1 G106.84-83.24	RXC J0043.4-2037	00:43:24.23	-20:37:33.7	0.292	9.1	0.0498	0.0034	9409
389	PSZ1 G107.14+65.29	RXC J1332.7+5032	13:32:38.51	+50:33:43.1	0.279	7.9	0.0318	0.0018	2213
407	PSZ1 G110.99+31.74	RXC J1703.8+7838	17:03:00.60	+78:38:59.4	0.058	6.3	0.0293	0.0003	1386,16129,16514,16515,16516
411	PSZ1 G112.48+57.02	RXC J1336.1+5912	13:36:08.42	+59:12:23.1	0.070	3.1	0.0517	0.0024	12282
415	PSZ1 G113.84+44.33	RXC J1414.2+7115	14:13:54.32	+71:17:40.0	0.224	5.0	0.0292	0.0041	15129

INDEX	NAME	Alt. Name	R.A. _x	Dec. _x	Redshift	M_{500} $10^{14}M_{\odot}$	c	σ_c	Obs. ID
417	PSZ1 G114.29+64.91	RXC J1315.1+5149	13:15:05.08	+51:49:03.4	0.283	5.9	0.0486	0.0020	15123,16126
419	PSZ1 G114.78-33.72	RXC J0020.6+2840	00:20:37.55	+28:39:32.8	0.093	3.8	0.0492	0.0037	15164
422	PSZ1 G114.99+70.36	RXC J1306.9+4633	13:06:49.79	+46:33:29.8	0.225	6.1	0.0417	0.0034	11725,3244
423	PSZ1 G115.20-72.07	RXC J0041.8-0918	00:41:50.26	-09:18:11.3	0.055	4.9	0.1483	0.0004	15173,15174,16263,16264,904
454	PSZ1 G124.20-36.47	RXC J0055.9+2622	00:55:50.42	+26:24:35.9	0.197	7.2	0.1705	0.0014	13458,13459,15578,15581,3233
459	PSZ1 G125.68-64.12	RXC J0056.3-0112	00:56:20.16	-01:14:34.1	0.044	3.3	0.0220	0.0005	4180,7918
460	PSZ1 G125.72+53.87	RXC J1236.9+6311	12:36:58.66	+63:11:13.3	0.301	5.9	0.0565	0.0030	15127,7938
482	PSZ1 G134.73+48.89	RXC J1133.2+6622	11:33:14.64	+66:22:48.0	0.115	3.5	0.0663	0.0023	0083150401
502	PSZ1 G139.17+56.37	RXC J1142.5+5832	11:42:23.70	+58:31:53.8	0.321	7.1	0.0231	0.0026	15136
503	PSZ1 G139.61+24.20		06:21:48.95	+74:42:04.8	0.266	7.0	0.1744	0.0050	15139,15297
513	PSZ1 G143.28+65.22	RXC J1159.2+4947	11:59:14.83	+49:47:33.2	0.350	7.3	0.0384	0.0045	15119
530	PSZ1 G149.21+54.17	RXC J1058.4+5647	10:58:26.86	+56:47:37.3	0.136	6.2	0.0302	0.0026	13376
532	PSZ1 G149.55-84.16	RXC J0102.7-2152	01:02:41.72	-21:52:53.9	0.056	3.0	0.2395	0.0012	13518,3183,3710,9897
533	PSZ1 G149.75+34.68	RXC J0830.9+6551	08:30:58.87	+65:50:17.4	0.181	8.2	0.0498	0.0019	3586
535	PSZ1 G150.56+58.32	RXC J1115.2+5320	11:15:15.09	+53:19:58.0	0.469	7.9	0.0318	0.0036	3253,5008,5350
558	PSZ1 G159.81-73.47	RXC J0131.8-1336	01:31:52.76	-13:36:41.4	0.206	8.1	0.0468	0.0025	3579,522
560	PSZ1 G161.39+26.24	RXC J0721.3+5547	07:21:31.44	+55:45:43.2	0.038	2.0	0.0678	0.0008	0504320101
567	PSZ1 G163.69+53.52	RXC J1022.5+5006	10:22:28.25	+50:06:22.3	0.158	4.9	0.0595	0.0037	15105
572	PSZ1 G165.06+54.13	RXC J1023.6+4907	10:23:39.84	+49:08:37.7	0.143	4.6	0.0458	0.0031	15114
578	PSZ1 G166.11+43.40	RXC J0917.8+5143	09:17:53.55	+51:43:42.3	0.217	7.0	0.0394	0.0024	5006
582	PSZ1 G167.64+17.63	RXC J0638.1+4747	06:38:03.83	+47:47:53.4	0.173	6.5	0.0334	0.0029	14388
608	PSZ1 G180.25+21.03	RXC J0717.5+3745	07:17:31.97	+37:45:28.7	0.546	11.	0.0291	0.0017	1655,4200
610	PSZ1 G180.56+76.66	RXC J1157.3+3336	11:57:17.39	+33:36:38.4	0.213	6.0	0.1167	0.0038	11724,538
617	PSZ1 G182.55+55.83	RXC J1017.0+3902	10:17:03.6	+39:02:48.06	0.206	5.7	0.1049	0.0021	903
628	PSZ1 G186.37+37.26	RXC J0842.9+3621	08:42:57.78	+36:21:59.4	0.282	11.	0.0349	0.0023	4217
654	PSZ1 G195.60+44.03	RXC J0920.4+3030	09:20:26.83	+30:29:36.2	0.295	6.3	0.0338	0.0033	15128,534
655	PSZ1 G195.78-24.29	RXC J0454.1+0255	04:54:06.71	+02:54:26.3	0.202	7.0	0.0300	0.0013	4215
676	PSZ1 G205.07-62.94		02:46:26.64	-20:33:10.8	0.310	7.3	0.0189	0.0022	0674380501
681	PSZ1 G205.94-39.46	RXC J0417.5-1154	04:17:34.74	-11:54:34.0	0.442	11.	0.1761	0.0076	3270
686	PSZ1 G208.59-26.00	RXC J0510.7-0801	05:10:47.48	-08:01:35.6	0.219	7.3	0.0495	0.0030	14011
688	PSZ1 G208.80-30.67	RXC J0454.1-1014	04:54:06.90	-10:13:18.7	0.247	6.9	0.0412	0.0015	12880,13190,430,901
700	PSZ1 G212.97-84.04	RXC J0118.1-2658	01:18:11.08	-26:57:57.4	0.227	6.1	0.0395	0.0030	9429
715	PSZ1 G216.60+47.00	RXC J0949.8+1707	09:49:51.73	+17:07:06.8	0.382	8.2	0.0547	0.0048	3274
726	PSZ1 G218.83+35.49	RXC J0909.1+1059	09:09:12.72	+10:58:27.9	0.175	5.5	0.0800	0.0029	924
744	PSZ1 G223.91-60.09	RXC J0307.0-2840	03:07:01.98	-28:39:56.2	0.253	6.7	0.1473	0.0053	9414
758	PSZ1 G226.19+76.78	RXC J1155.3+2324	11:55:17.95	+23:24:19.0	0.142	5.9	0.1023	0.0011	1661,5003,537
759	PSZ1 G226.19-21.92	RXC J0552.8-2103	05:52:51.43	-21:03:14.5	0.098	4.2	0.0474	0.0030	15307
772	PSZ1 G229.23-17.23	RXC J0616.3-2156	06:16:24.73	-21:56:15.6	0.171	5.9	0.0337	0.0030	15100
773	PSZ1 G229.70+77.97	RXC J1201.3+2306	12:01:15.52	+23:06:19.4	0.268	7.7	0.0236	0.0023	11762,16279
774	PSZ1 G229.92+15.28	RXC J0817.4-0730	08:17:25.95	-07:30:34.0	0.070	4.6	0.0743	0.0009	2211
796	PSZ1 G236.93-26.65	RXC J0547.6-3152	05:47:36.60	-31:52:07.1	0.148	5.2	0.0425	0.0021	9419
801	PSZ1 G239.29+24.75	RXC J0909.1-0939	09:09:17.12	-09:41:12.6	0.054	6.6	0.0321	0.0005	577
802	PSZ1 G239.30-26.01	RXC J0553.4-3342	05:53:28.45	-33:42:33.3	0.430	9.3	0.0424	0.0020	12244,5813
815	PSZ1 G241.75-30.89	RXC J0532.9-3701	05:32:55.42	-37:01:37.6	0.270	6.7	0.0770	0.0037	15112
816	PSZ1 G241.76-24.01	RXC J0605.8-3518	06:05:53.95	-35:18:07.7	0.139	5.4	0.2335	0.0065	15315
818	PSZ1 G241.98+14.87	RXC J0841.9-1729	08:41:52.03	-17:27:50.4	0.168	6.4	0.0385	0.0020	13378,15316
822	PSZ1 G243.14-73.87	RXC J0159.0-3412	01:59:02.69	-34:12:57.6	0.409	7.6	0.0300	0.0061	5818
824	PSZ1 G243.60+67.74	RXC J1132.8+1428	11:32:51.92	+14:27:11.4	0.083	4.1	0.0493	0.0028	14387

INDEX	NAME	Alt. Name	R.A. _χ	Dec. _χ	Redshift	M_{500} $10^{14}M_{\odot}$	c	σ_c	Obs. ID
826	PSZ1 G244.35-32.15	RXC J0528.9-3927	05:28:52.98	-39:28:15.4	0.283	7.3	0.1139	0.0024	15177,15658,4994
829	PSZ1 G244.67+32.47	RXC J0945.4-0839	09:45:27.04	-08:39:24.9	0.153	5.0	0.0321	0.0027	15109
838	PSZ1 G246.53-26.07	RXC J0601.7-3959	06:02:11.65	-39:56:55.9	0.046	2.2	0.0279	0.0024	3202,3450
840	PSZ1 G247.19-23.31	RXC J0616.5-3948	06:16:32.18	-39:47:47.2	0.151	4.2	0.0530	0.0042	15126
857	PSZ1 G250.92-36.24	RXC J0510.2-4519	05:10:17.06	-45:19:10.8	0.200	5.9	0.0663	0.0043	15111
862	PSZ1 G252.99-56.06	RXC J0317.9-4414	03:17:57.68	-44:14:18.2	0.075	3.0	0.2612	0.0018	13135,6972,7323,7324
868	PSZ1 G253.49-33.73	RXC J0525.8-4715	05:25:48.96	-47:15:10.7	0.191	4.8	0.0690	0.0042	15122
877	PSZ1 G255.60-46.18	SPT-CLJ0411-4819	04:11:16.40	-48:18:53.8	0.423	6.8	0.0917	0.0047	13396,16355,17536
880	PSZ1 G256.55-65.69	RXC J0225.9-4154	02:25:53.03	-41:54:56.2	0.219	5.8	0.1338	0.0064	15110
882	PSZ1 G257.32-22.19	RXC J0637.3-4828	06:37:14.66	-48:28:18.2	0.202	4.8	0.0898	0.0051	15125
889	PSZ1 G260.00-63.45	RXC J0232.2-4420	02:32:18.70	-44:20:46.9	0.283	6.8	0.1423	0.0126	4993
898	PSZ1 G262.27-35.38	RXC J0516.6-5430	05:16:36.65	-54:30:49.5	0.295	9.0	0.0235	0.0028	15099,9331
901	PSZ1 G262.72-40.92		04:38:17.11	-54:19:24.9	0.421	7.5	0.0791	0.0055	12259
904	PSZ1 G263.14-23.42	RXC J0638.7-5358	06:38:48.53	-53:58:26.6	0.226	6.7	0.1116	0.0035	9420
905	PSZ1 G263.19-25.22	RXC J0627.2-5428	06:26:47.69	-54:32:48.2	0.050	2.6	0.0529	0.0020	4944
907	PSZ1 G263.68-22.55	RXC J0645.4-5413	06:45:28.62	-54:13:40.7	0.164	7.8	0.0749	0.0037	15301
912	PSZ1 G264.62-51.07	RXC J0330.8-5228	03:29:50.57	-52:34:50.9	0.439	5.7	0.0296	0.0041	893
914	PSZ1 G265.02-48.96	RXC J0342.8-5338	03:42:46.93	-53:36:39.2	0.059	4.2	0.0276	0.0005	3201,3712
920	PSZ1 G266.02-21.23	RXC J0658.5-5556	06:58:20.12	-55:56:30.2	0.296	12.	0.0568	0.0006	3184,4984,4985,4986,5355,5356,5357,5358,5361,554
924	PSZ1 G266.85+25.06	RXC J1023.8-2715	10:23:50.25	-27:15:21.6	0.254	7.6	0.2289	0.0030	9400
931	PSZ1 G269.28-49.89	RXC J0328.6-5542	03:28:36.85	-55:43:09.2	0.085	3.1	0.0638	0.0034	15313
941	PSZ1 G271.48-56.57	ACO S 295	02:45:24.84	-53:01:42.9	0.300	6.5	0.0451	0.0011	12260,16127,16282,16524,16525
944	PSZ1 G272.08-40.16	RXC J0431.4-6126	04:31:13.25	-61:27:14.0	0.058	6.7	0.0362	0.0007	899
951	PSZ1 G273.54+63.23	RXC J1200.4+0320	12:00:24.74	+03:20:37.9	0.133	5.6	0.0240	0.0019	15188,15306
960	PSZ1 G278.58+39.15	RXC J1131.9-1955	11:31:54.42	-19:55:42.3	0.307	8.8	0.0734	0.0058	3276
971	PSZ1 G280.21+47.83	RXC J1149.7-1219	11:49:47.39	-12:18:56.2	0.155	5.4	0.0293	0.0030	15311
980	PSZ1 G282.45+65.18	RXC J1217.6+0339	12:17:41.06	+03:39:18.4	0.076	4.6	0.0380	0.0015	4184
984	PSZ1 G284.43+52.44	RXC J1206.2-0848	12:06:12.12	-08:48:02.2	0.441	10.	0.0858	0.0041	3277
988	PSZ1 G285.63+72.72	RXC J1230.7+1033	12:30:47.58	+10:33:11.9	0.165	5.6	0.0376	0.0029	12254
993	PSZ1 G286.27-38.39		03:59:09.12	-72:04:33.6	0.307	6.0	0.0240	0.0033	0656200501
994	PSZ1 G286.60-31.23		05:31:28.81	-75:10:36.2	0.209	5.2	0.0349	0.0034	15115
1006	PSZ1 G287.95-32.98		04:59:45.36	-75:48:32.4	0.25	5.8	0.0278	0.0025	0762800101
1009	PSZ1 G288.26+39.94	RXC J1203.2-2131	12:03:17.04	-21:32:20.4	0.199	7.3	0.0251	0.0015	0652010101
1011	PSZ1 G288.63-37.67	RXC J0352.4-7401	03:52:32.37	-74:02:09.3	0.127	6.4	0.0375	0.0028	13380
1032	PSZ1 G294.68-37.01	RXC J0303.7-7752	03:03:40.73	-77:52:45.7	0.274	6.9	0.0380	0.0027	15113
1037	PSZ1 G295.34+23.34	RXC J1215.4-3900	12:15:26.70	-39:01:38.2	0.119	4.3	0.0245	0.0022	15140,15310
1038	PSZ1 G295.60-51.95		01:33:26.88	-64:34:08.4	0.333	6.3	0.0439	0.0067	0762800301
1041	PSZ1 G296.42-32.49	RXC J0351.1-8212	03:51:31.80	-82:13:10.7	0.061	2.5	0.0524	0.0024	16283,8272
1046	PSZ1 G297.94-67.76	SPT-CLJ0102-49151	01:02:58.27	-49:16:27.1	0.870	8.7	0.1155	0.0023	12258,14022,14023
1057	PSZ1 G303.73+33.69	RXC J1254.6-2913	12:54:40.64	-29:13:40.0	0.054	3.2	0.1850	0.0050	8268
1062	PSZ1 G304.44+32.45	RXC J1257.2-3022	12:57:21.98	-30:21:47.7	0.055	3.0	0.0526	0.0025	10745
1065	PSZ1 G304.86-41.40		00:28:02.66	-75:37:52.7	0.409	7.5	0.0340	0.0037	14390
1066	PSZ1 G304.91+45.46	RXC J1257.1-1724	12:57:11.80	-17:24:31.8	0.047	3.8	0.0784	0.0008	2206,7922
1071	PSZ1 G305.88-44.56		00:23:39.12	-72:24:03.6	0.300	6.0	0.0400	0.0032	0679180301
1078	PSZ1 G306.71+61.04	RXC J1258.6-0145	12:58:41.45	-01:45:43.7	0.084	4.0	0.1110	0.0006	5822,5823,6356,6357,6358,7242
1079	PSZ1 G306.77+58.62	RXC J1259.3-0411	12:59:22.16	-04:11:50.1	0.084	5.1	0.0798	0.0021	4185
1095	PSZ1 G311.98+30.73	RXC J1327.9-3130	13:27:56.88	-31:29:45.6	0.048	4.4	0.0557	0.0004	0107260101
1100	PSZ1 G312.64+35.09	RXC J1326.9-2710	13:26:58.24	-27:10:55.2	0.045	2.9	0.0215	0.0010	4186

INDEX	NAME	Alt. Name	R.A. _X	Dec. _X	Redshift	M_{500} $10^{14}M_{\odot}$	c	σ_c	Obs. ID
1105	PSZ1 G313.33+61.13	RXC J1311.5-0120	13:11:29.52	-01:20:24.4	0.183	8.8	0.1168	0.0015	1663,5004,540
1109	PSZ1 G313.88-17.12	RXC J1601.7-7544	16:01:49.10	-75:45:19.3	0.152	7.5	0.0814	0.0027	14386
1117	PSZ1 G315.69-18.05	RXC J1631.6-7507	16:31:21.25	-75:06:51.5	0.104	6.4	0.0269	0.0016	13377,15317
1118	PSZ1 G316.33+28.55	RXC J1347.4-3250	13:47:28.32	-32:51:57.6	0.039	4.6	0.0626	0.0004	0086950201
1126	PSZ1 G321.98-47.96	RXC J2249.9-6425	22:49:56.87	-64:25:48.3	0.093	4.3	0.0541	0.0015	4973
1134	PSZ1 G324.05+48.79	RXC J1347.5-1144	13:47:30.60	-11:45:09.6	0.451	10.	0.2448	0.0026	3592,507
1136	PSZ1 G324.51-44.98	RXC J2218.0-6511	22:18:00.10	-65:10:52.5	0.095	3.5	0.1183	0.0054	15314
1139	PSZ1 G325.70+17.31		14:47:33.89	-40:20:38.5	0.315	7.4	0.0373	0.0052	15298
1157	PSZ1 G332.21-46.38	RXC J2201.9-5956	22:01:52.91	-59:56:44.8	0.097	5.9	0.0536	0.0008	7920
1160	PSZ1 G332.87-19.26	RXC J1813.3-6127	18:13:13.20	-61:27:04.0	0.146	5.8	0.0459	0.0031	14389
1164	PSZ1 G335.57-46.47	RXC J2154.1-5751	21:54:04.18	-57:52:03.9	0.075	4.1	0.0435	0.0023	8269
1165	PSZ1 G336.61-55.43	RXC J2246.3-5243	22:46:28.61	-52:45:45.3	0.096	4.3	0.0293	0.0025	15304
1182	PSZ1 G340.37+60.57	RXC J1401.0+0252	14:01:01.97	+02:52:43.4	0.252	8.4	0.2624	0.0030	495
1184	PSZ1 G340.86-33.36	RXC J2012.5-5649	20:12:42.07	-56:50:48.8	0.055	5.7	0.0296	0.0002	513,5751,5752,5753,6292,6295,6296,889
1185	PSZ1 G340.94+35.10	RXC J1459.4-1811	14:59:28.99	-18:10:45.0	0.235	7.7	0.2723	0.0037	9428
1190	PSZ1 G342.33-34.92	RXC J2023.4-5535	20:23:21.39	-55:35:49.8	0.231	6.6	0.0351	0.0034	15108
1192	PSZ1 G342.83-30.47	RXC J1952.2-5503	19:52:13.41	-55:03:13.6	0.059	3.0	0.0279	0.0024	15308
1200	PSZ1 G346.61+35.06	RXC J1514.9-1523	15:15:03.13	-15:22:46.1	0.222	8.3	0.0163	0.0015	15175
1201	PSZ1 G347.20-27.36	RXC J1934.7-5053	19:34:52.46	-50:52:34.6	0.237	6.4	0.0286	0.0028	15120
1207	PSZ1 G348.92-67.38	ACO S 1121	23:25:11.39	-41:12:12.4	0.358	5.0	0.0623	0.0090	13405
1208	PSZ1 G349.46-59.92	RXC J2248.7-4431	22:48:43.90	-44:31:50.0	0.347	11.	0.0625	0.0020	4966
1214	PSZ1 G352.35-77.66	RXC J0006.0-3443	00:06:00.00	-34:43:19.2	0.114	3.7	0.0273	0.0016	0201903801
1216	PSZ1 G355.07+46.20	RXC J1504.1-0248	15:04:07.43	-2:48:15.94	0.215	6.9	0.3392	0.0025	5793
1218	PSZ1 G356.18-76.06	RXC J2357.0-3445	23:57:00.72	-34:45:36.0	0.047	2.3	0.1284	0.0068	0109950201
1224	PSZ1 G358.96-67.26	RXC J2315.7-3746	23:15:46.32	-37:47:49.2	0.178	5.4	0.0480	0.0037	0762800501

Table 1: Properties of the clusters in our *Planck* sample. Col. [1] is the INDEX in the PSZ1 catalogue, col. [2] the *Planck* name, col. [3] provides an alternative name, Cols. [4] and [5] are the coordinates of the X-ray peak that we used to measure the concentration parameter, col. [6] and col[7] are the redshift and mass as provided in the *Planck* catalogue, col. [8] and col. [9] are the concentration parameter and its error, while in col [10] we list the ID of the observations used in our analysis (those starting with “0” are *XMM-Newton* data).

NAME	R.A. _x	Dec. _x	Redshift	M_{500} $10^{14}M_{\odot}$	c	σ_c	Obs. ID
A1914	14:26:03.12	+37:49:24.9	0.17	8.08	0.0626	0.0014	3593
A209	01:31:52.76	-13:36:41.4	0.21	5.71	0.0482	0.0025	3579 522
A586	07:32:20.61	+31:37:49.4	0.17	5.99	0.0835	0.0028	11723 530
ABELL1689	13:11:29.52	-01:20:24.4	0.18	9.46	0.1188	0.0016	6930
ABELL1758	13:32:38.49	+50:33:35.0	0.28	5.41	0.0263	0.0016	2213
ABELL1835	14:01:02.10	+02:52:45.4	0.25	11.8	0.2500	0.0029	6880
ABELL2163	16:15:46.06	-06:09:06.0	0.21	12.3	0.0224	0.0006	1653
ABELL2204	16:32:46.94	+05:34:32.1	0.15	9.60	0.3051	0.0013	7940
ABELL2219	16:40:21.46	+46:42:27.4	0.23	8.78	0.0283	0.0007	7892
ABELL2261	17:22:27.30	+32:07:55.4	0.22	7.58	0.1143	0.0030	5007
ABELL2390	21:53:36.81	+17:41:45.2	0.23	9.22	0.1249	0.0011	4193
ABELL2631	23:37:38.08	+00:16:02.2	0.28	6.41	0.0308	0.0039	11728 3248
ABELL2667	23:51:39.37	-26:05:01.8	0.23	9.18	0.1648	0.0040	2214
ABELL2744	00:14:19.04	-30:23:30.0	0.31	9.35	0.0223	0.0009	8477 8557
ABELL2813	00:43:24.37	-20:37:33.8	0.29	5.83	0.0489	0.0032	9409
ABELL3088	03:07:01.82	-28:39:56.4	0.25	5.49	0.1389	0.0051	9414
ABELL520	04:54:05.11	+02:53:37.0	0.2	6.86	0.0305	0.0016	4215
ABELL521	04:54:06.56	-10:13:14.9	0.25	6.38	0.0391	0.0023	901
ABELL611	08:00:56.83	+36:03:23.4	0.29	5.56	0.1232	0.0036	3194
ABELL665	08:30:58.52	+65:50:24.7	0.18	7.42	0.0485	0.0018	3586
ABELL697	08:42:57.60	+36:21:59.4	0.28	7.74	0.0350	0.0022	4217
ABELL773	09:17:51.21	+51:43:38.3	0.22	5.97	0.0385	0.0023	5006 533
Abell1682	13:06:49.79	+46:33:29.8	0.23	5.77	0.0427	0.0034	11725 3244
Abell2146	15:56:14.83	+66:20:49.1	0.23	5.68	0.1215	0.0009	10464
Abell2552	23:11:33.25	+03:38:08.2	0.3	7.04	0.0629	0.0032	11730
IRAS09104+4109	09:13:45.57	+40:56:28.9	0.44	6.62	0.2998	0.0056	10445
MACS-J0111.5+0855	01:11:31.60	+08:55:41.9	0.49	6.22	0.1609	0.0167	3256
MACS-J2129.4-0741	21:29:25.68	-07:41:23.7	0.59	6.04	0.0576	0.0051	3199 3595
MACS-J2243.3-0935	22:43:21.19	-09:35:37.2	0.45	8.14	0.0238	0.0032	3260
MACS1108.8+0906	11:08:55.82	+09:05:53.6	0.47	5.07	0.0394	0.0041	5009
MACS1427+44	14:27:16.09	+44:07:30.3	0.49	6.92	0.2531	0.0070	9380
MACS1427-25	14:27:39.44	-25:21:01.6	0.32	6.45	0.2735	0.0076	3279 9373
MACS911.2+1746	09:11:10.90	+17:46:28.9	0.51	5.55	0.0381	0.0044	3587 5012
MACSJ0011.7-1523	00:11:42.89	-15:23:20.6	0.38	6.41	0.1532	0.0046	3261 6105
MACSJ0025.4-1222	00:25:29.43	-12:22:40.5	0.58	6.42	0.0309	0.0019	10413
MACSJ0035.4-2015	00:35:26.31	-20:15:46.8	0.35	6.02	0.0519	0.0032	3262
MACSJ0140.0-0555	01:40:01.49	-05:55:11.0	0.45	6.54	0.0503	0.0049	5013 12243
MACSJ0152.5-2852	01:52:34.45	-28:53:37.8	0.41	7.66	0.1112	0.0078	3264
MACSJ0159.0-3412	01:59:04.00	-34:12:49.7	0.41	5.53	0.0212	0.0055	5818
MACSJ0159.8-0849	01:59:49.30	-08:49:58.5	0.41	7.56	0.2194	0.0045	6106
MACSJ0242.5-2132	02:42:35.99	-21:32:26.6	0.31	7.67	0.3821	0.0111	3266
MACSJ0257.1-2325	02:57:08.73	-23:26:08.0	0.51	6.09	0.0935	0.0049	1654 3581
MACSJ0257.6-2209	02:57:40.97	-22:09:17.4	0.32	5.74	0.1095	0.0058	3267
MACSJ0308.9+2645	03:08:56.06	+26:45:42.5	0.36	6.01	0.0514	0.0031	3268
MACSJ0326.8-0043	03:26:49.88	-00:43:51.8	0.45	6.43	0.3432	0.0162	5810
MACSJ0329.6-0211	03:29:41.60	-02:11:45.5	0.45	5.94	0.2747	0.0060	6108
MACSJ0358.8-2955	03:58:54.30	-29:55:33.3	0.43	8.48	0.0837	0.0025	12300 13194 11719
MACSJ0404.6+1109	04:04:33.46	+11:08:00.0	0.36	6.44	0.0425	0.0064	3269
MACSJ0416.1-2403	04:16:09.22	-24:04:02.3	0.4	6.20	0.0491	0.0010	10446
MACSJ0417.5-1154	04:17:34.60	-11:54:30.0	0.44	11.0	0.1571	0.0070	11759
MACSJ0429.6-0253	04:29:35.97	-02:53:08.1	0.4	6.78	0.2924	0.0097	3271
MACSJ0451.9+0006	04:51:54.39	+00:06:19.4	0.43	5.04	0.0638	0.0092	5815
MACSJ0455.2+0657	04:55:17.11	+06:57:47.7	0.45	7.00	0.0997	0.0104	5812
MACSJ0520.7-1328	05:20:41.93	-13:28:49.7	0.34	6.39	0.0951	0.0055	3272
MACSJ0547.0-3904	05:47:01.54	-39:04:27.0	0.32	5.51	0.2963	0.0106	3273
MACSJ0553.4-3342	05:53:28.45	-33:42:33.3	0.43	6.08	0.0351	0.0018	5813
MACSJ0717.5+3745	07:17:31.97	+37:45:28.7	0.55	8.52	0.0277	0.0018	4200
MACSJ0744.8+3927	07:44:52.80	+39:27:26.0	0.7	7.52	0.1663	0.0049	6111
MACSJ0949.8+1708	09:49:51.73	+17:07:06.8	0.38	8.37	0.0533	0.0048	3274

NAME	R.A. _x	Dec. _x	Redshift	M_{500} $10^{14}M_{\odot}$	c	σ_c	Obs. ID
MACSJ1006.9+3200	10:06:54.90	+32:01:33.0	0.4	5.08	0.0423	0.0078	5819
MACSJ1105.7-1014	11:05:46.01	-10:14:36.6	0.41	5.29	0.0468	0.0074	5817
MACSJ1115.2+5320	11:15:14.89	+53:19:56.1	0.47	5.03	0.0521	0.0037	5008
MACSJ1115.8+0129	11:15:51.87	+01:29:56.2	0.35	7.49	0.1993	0.0041	9375
MACSJ1131.8-1955	11:31:54.84	-19:55:46.2	0.31	6.71	0.0664	0.0054	3276
MACSJ1149.5+2223	11:49:35.28	+22:24:04.8	0.54	6.43	0.0316	0.0032	1656 3589
MACSJ1206.2-0847	12:06:12.12	-08:48:02.3	0.44	7.19	0.0856	0.0041	3277
MACSJ1226.8+2153	12:26:51.05	+21:49:50.0	0.44	4.79	0.0932	0.0036	3590
MACSJ1311.0-0310	13:11:01.45	-03:10:39.8	0.49	6.19	0.1670	0.0052	6110
MACSJ1319.9+7003	13:20:08.12	+70:04:37.0	0.33	5.86	0.0883	0.0089	3278
MACSJ1359.1-1929	13:59:10.30	-19:29:25.4	0.45	5.31	0.2751	0.0088	9378
MACSJ1621.3+3810	16:21:24.87	+38:10:07.7	0.46	5.68	0.2339	0.0060	6109
MACSJ1731.6+2252	17:31:38.21	+22:51:49.3	0.39	7.15	0.0154	0.0031	3281
MACSJ1931.8-2634	19:31:49.59	-26:34:34.3	0.35	8.41	0.3017	0.0081	9382
MACSJ2046.0-3430	20:46:00.55	-34:30:15.3	0.42	5.49	0.3067	0.0077	9377
MACSJ2049.9-3217	20:49:55.25	-32:16:51.6	0.32	5.42	0.0457	0.0038	3283
MACSJ2211.7-0349	22:11:46.13	-03:49:47.5	0.4	8.01	0.0970	0.0041	3284
MACSJ2214.9-1359	22:14:57.13	-14:00:16.6	0.5	6.52	0.0502	0.0039	3259 5011
MACSJ2228+2036	22:28:33.72	+20:37:16.6	0.41	7.47	0.0556	0.0048	3285
MACSJ2229.7-2755	22:29:45.18	-27:55:37.8	0.32	6.33	0.3643	0.0114	3286 9374
MACSJ2245.0+2637	22:45:04.48	+26:38:03.3	0.3	6.26	0.1846	0.0084	3287
MS0016.9+1609	00:18:33.75	+16:26:11.6	0.55	6.73	0.0380	0.0022	520
MS0451.6-0305	04:54:10.93	-03:00:55.9	0.54	7.60	0.0429	0.0023	529
MS0735.6+7421	07:41:44.13	+74:14:39.9	0.22	5.72	0.1866	0.0031	10470
MS1455.0+2232	14:57:15.07	+22:20:32.7	0.26	7.10	0.2832	0.0029	4192
MS2137.3-2353	21:40:15.17	-23:39:39.7	0.31	6.50	0.3503	0.0111	4974
RBS0797	09:47:12.86	+76:23:13.1	0.35	8.90	0.3189	0.0035	2202
RCS1447+0828	14:47:25.87	+08:28:24.8	0.38	9.73	0.3132	0.0070	10481
RXCJ0528.9-3927	05:28:52.98	-39:28:15.4	0.28	8.22	0.1139	0.0024	4994
RXCJ1023.8-2715	10:23:50.25	-27:15:21.6	0.25	8.68	0.2173	0.0029	9400
RXCJ1459.4-1811	14:59:28.99	-18:10:45.0	0.23	7.10	0.2551	0.0036	9428
RXJ0437.1+0043	04:37:09.47	+00:43:55.6	0.28	6.14	0.1481	0.0038	11729
RXJ0439.0+0715	04:39:00.37	+07:16:06.1	0.24	5.48	0.0993	0.0035	3583
RXJ0647.7+7015	06:47:50.88	+70:14:50.6	0.59	7.20	0.0626	0.0043	3196 3584
RXJ1347.5-1145	13:47:30.60	-11:45:09.6	0.45	13.5	0.2421	0.0026	3592
RXJ1423.8+2404	14:23:47.96	+24:04:43.8	0.54	5.90	0.3159	0.0045	1657
RXJ1504.1-0248	15:04:07.69	-02:48:15.9	0.22	13.9	0.3196	0.0024	5793
RXJ1532.9+3021	15:32:53.89	+30:20:59.8	0.36	8.05	0.2442	0.0052	1665
RXJ1720.1+2638	17:20:09.92	+26:37:30.9	0.16	7.12	0.2320	0.0033	3224 4361
RXJ1720.2+3536	17:20:16.69	+35:36:26.1	0.39	6.94	0.2244	0.0052	3280 6107
RXJ2014.8-2430	20:14:51.49	-24:30:22.8	0.15	7.90	0.3286	0.0034	11757
RXJ2129.6+0005	21:29:39.99	+00:05:20.1	0.23	7.81	0.2116	0.0070	9370
Z7215	15:01:22.73	+42:20:44.7	0.29	5.37	0.0390	0.0046	7899
ZWCL3146	10:23:39.60	+04:11:12.1	0.29	11.4	0.2213	0.0027	909 9371
ZwCl0348	01:06:49.44	+01:03:23.0	0.25	5.64	0.3577	0.0048	10465

Table 2: Properties of the clusters in the ME-MACS sample. Col. [1] is the cluster name, Cols. [2] and [3] are the coordinates of the X-ray peak that we used to measure the concentration parameter, col. [4] is the redshift of the clusters and col[5] is its mass calculated from the X-ray luminosity in (Mann & Ebeling 2012), col. [6] and col. [7] are the concentration parameter and its error, while in col [8] we list the ID of the observations used in our analysis (those starting with “0” are *XMM-Newton* data).